

Contents

1	Introduction	2
2	Related Work	4
3	System Overview	5
4	Data Filtering and Curation	5
5	MeshGen	6
5.1	MeshGen Data Preparation	6
5.2	MeshGen Architecture	7
5.3	MeshGen Distillation	9
6	Geometry Post-Processing for Runtime Assets	9
6.1	Mesh Simplification	10
6.2	Hidden Face Removal	11
6.3	UV Unwrapping	11
6.4	Normal Map Baking	12
7	TextureGen	13
7.1	TextureGen Data Preparation	13
7.2	TextureGen Architecture	14
7.3	TextureGen Distillation	15
7.4	TextureGen Postprocessing	15
7.5	Geometric Condition Rendering	16
8	Latency Optimization	16
8.1	Kernel and Precision Optimization	16
8.2	Pipeline Optimization	16
8.3	Latency Results	18
9	Evaluation	18
9.1	AssetBench: General Object Generation	18
9.2	CharacterBench: Character Generation	19
9.3	Human Evaluation	21
10	Qualitative Results	23
11	Conclusion and Limitations	23

1 Introduction

3D assets are a key part of games, AR/VR, robotic simulation, and more. Yet, producing them remains a slow, manual process: artists must shape the geometry of the assets, optimize the mesh and polygon count to stay within a certain budget, unwrap the mesh for texturing, bake normals, and author the texture. The resulting assets can be excellent, but the workflow is slow and difficult to scale to the volume of content needed by existing and future applications.

Image-to-3D generation has the potential to change the economics of 3D content creation. In particular, recent work has made significant progress on the quality of generated 3D assets. Geometry models have improved shape fidelity and detail (Li et al., 2025; Zhao et al., 2025b; Xiang et al., 2025b; Lai et al., 2025b), while multi-view texture models have improved artistic quality and view consistency (Bensadoun et al., 2024; Cheng et al., 2025). However, while the generated assets may look good at a glance, they are often too complex to use in real-time applications, particularly on mobile devices. Generation speed can also frustrate users. A

useful generator must have a latency in the tens of seconds to support workflows where assets are proposed, assessed, and revised iteratively by creators.

We therefore consider the problem of generating *application-ready 3D asset* in *interactive creative workflows*. To be deployable, the assets must satisfy quality and efficiency bars sufficient for use in real-time applications, including mobile ones. To be useful in interactive workflows, the assets must be generated in seconds rather than minutes.

To this end, we introduce **AssetGen**, an image-to-3D system designed to meet these goals. As shown in [figure 1](#), AssetGen delivers a high-quality textured mesh with a controlled polygon budget, UV coordinates, and baked normals in approximately 30 seconds on H100 GPUs. A fast variant, AssetGen Flash, reduces latency to approximately 14 seconds to support previews in faster interactive and agentic creation loops.

The system consists of three stages. First, *MeshGen* predicts a dense, highly detailed 3D shape using a two-stage coarse-to-refine diffusion model. Second, a GPU-based post-processing stack converts the dense shape into a deployable mesh by simplifying and cleaning the geometry, removing hidden faces, unwrapping UVs, and baking tangent-space normals to preserve high-frequency surface details. Finally, *TextureGen* synthesizes several views of the textured appearance of the processed mesh and fuses them into a 2048px texture atlas using GPU-based upsampling, backprojection, blending, and 3D-aware inpainting.

A key novelty of AssetGen is that inference is optimized end-to-end. First, latency is reduced through model distillation in both the geometry and texture generation stages. For example, diffusion sampling in MeshGen is progressively distilled from 120 denoising steps down to just 30 steps, further doubling speed by also distilling Classifier-Free Guidance (CFG) in a single forward pass. TextureGen is accelerated in a similar manner. Several other engineering decisions remove further bottlenecks, including FlashAttention-3, graph compilation, selective low-precision execution, non-blocking transfers, GPU-resident geometry operations, and asynchronous serving, all reducing wall-clock latency without regressing asset quality. The result is a practical image-to-3D pipeline whose output is competitive with leading commercial systems while running at a latency suitable for creative iteration.

The faster version AssetGen Flash skips the MeshGen refinement step, reduces the texture resolution to 1024px omitting upsampling and using more aggressive distillation, including CFG distillation. While the visual quality is slightly reduced, the much faster generation speed makes interactive creation more fluid and enjoyable.

We validate AssetGen using quantitative benchmarks, qualitative comparisons, and blind human evaluations. In particular, we introduce new benchmarks and evaluation metrics that measure specific aspects of 3D generation, including, for example, how certain details such as faces and hands are reconstructed in 3D characters—something that was not assessed systematically before to the best of our knowledge. With this, we show that AssetGen achieves competitive asset quality against leading commercial systems while substantially reducing latency. To summarize, our contributions are threefold:

Deployable 3D asset generation at interactive rates. We refocus image-to-3D as the task of generating 3D assets that can be deployed as-is in real-time rendering engines, including on mobile platforms, while also meeting strict latency constraints to support iterative creative workflows.

End-to-end system optimization. To achieve these goals, we re-engineer the system as a whole. We optimize each component of the pipeline, including MeshGen and TextureGen distillation, mesh simplification, hidden-face removal, UV unwrapping, normal baking and texture backprojection, and inpainting. We introduce system optimizations, including minimizing I/O by running most operations on the same GPU and masking latency via parallelism whenever possible. We optimize for speed while maintaining the quality of the asset.

Asset-level quality-latency Pareto design. We introduce two practical configurations: the default AssetGen prioritizes visual quality with an end-to-end runtime of approximately 30 seconds, while AssetGen Flash prioritizes responsiveness and reaches sub-15-second latency.

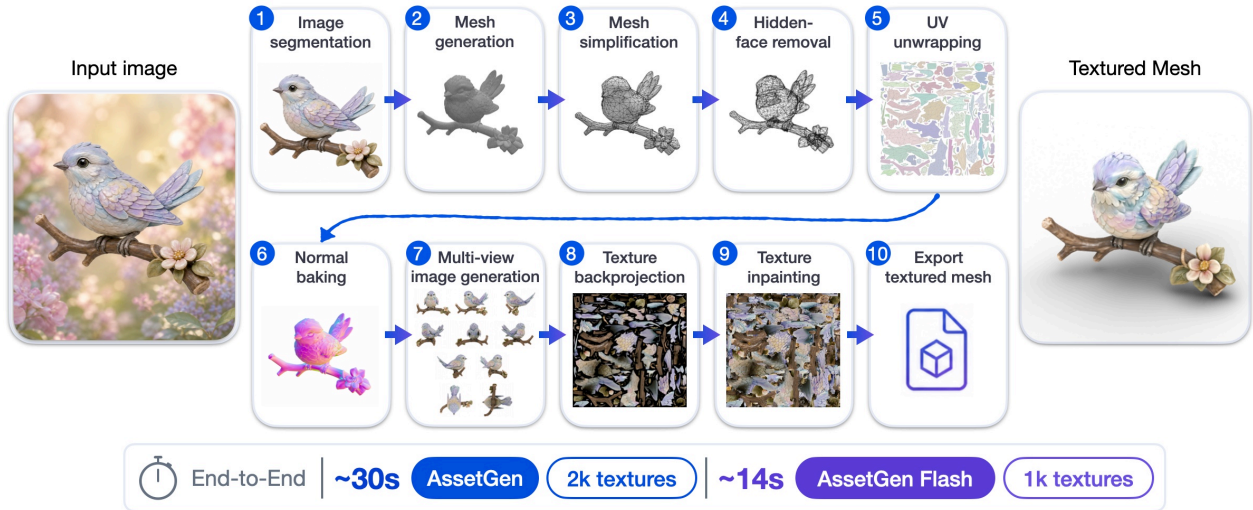


Figure 2 AssetGen converts a single input image into an export-ready textured mesh with two operating modes: **AssetGen** denotes the quality-oriented configuration that runs in ~ 30 seconds, and **AssetGen (Flash)** denotes the latency-oriented configuration that runs in approximately 14 seconds. Both produce the same asset contract: a simplified mesh with UVs, baked normals, and a texture atlas.

2 Related Work

3D Shape Generation. Neural 3D representations trade off rendering quality, extraction cost, and generative scalability. While radiance fields (Mildenhall et al., 2021; Müller et al., 2022), Gaussian splatting (Kerbl et al., 2023), and optimization-based lifting (Poole et al., 2022; Wang et al., 2023) prioritize high-quality view synthesis, interactive pipelines require fast, feed-forward geometric prediction (Tochilkin et al., 2024; Xu et al., 2024; Wang et al., 2024; Huang et al., 2025b). To balance generative scalability with straightforward mesh extraction, recent methods compress 3D data into compact latents like triplanes (Chan et al., 2022), wavelet features (Sanghi et al., 2024), primitives (Chen et al., 2025b), structured coordinates (Xiang et al., 2025a), and unordered vector sets (Zhang et al., 2023).

Building on native 3D diffusion models that learn robust priors directly in these spaces (Zhao et al., 2023; Zhang et al., 2024; Wu et al., 2024; Xiang et al., 2025b; Li et al., 2025; Zhao et al., 2025b), AssetGen adopts a distilled (Lai et al., 2025b), two-stage coarse-to-refine VecSet architecture (Lai et al., 2025a). This design provides a compact target for rapid diffusion while supporting the extraction of dense implicit surfaces (Park et al., 2019; Mescheder et al., 2019) necessary for normal baking. While an emerging family of approaches predicts mesh topology and edge flow directly (Siddiqui et al., 2024; Zhao et al., 2025a; Hao et al., 2024; Li et al., 2026; Xu et al., 2026; Wang et al., 2026; Lei et al., 2026; Lionar et al., 2025; Luo et al., 2026; He et al., 2025), our system focuses on the pipeline of dense implicit generation followed by explicit processing. Finally, to ensure high-quality geometry extraction and reliable SDF supervision from curated datasets (Li et al., 2025; ByteDance Seed3D Team, 2026), our data pipeline extends established sign-estimation techniques (Newcombe et al., 2011; Huang et al., 2020; Barill et al., 2018) with a boundary-aware flood-fill formulation to handle the open boundaries and inconsistent winding common in real-world assets.

Multi-View Texture Synthesis and Acceleration. Texture generation has evolved from sequential painting (Richardson et al., 2023; Chen et al., 2023; Zeng et al., 2024) to synchronized multi-view synthesis (Liu et al., 2023a, 2024; Shi et al., 2024; Long et al., 2024; Voleti et al., 2024; Li et al., 2024; Tang et al., 2023, 2024; Cheng et al., 2025; Bensadoun et al., 2024; Shao et al., 2025). In recent pipelines, these synchronized views are mapped onto explicit surfaces via geometric conditioning and specialized attention mechanisms (Xiang et al., 2025c; Sarafianos et al., 2025; Huang et al., 2025a; Hasselgren et al., 2026; Hunyuan3D et al., 2025; He et al., 2020; Ye et al., 2023). However, deploying the underlying diffusion transformers (Peebles and Xie, 2023; Bao et al., 2023; Esser et al., 2024; Liu et al., 2022) interactively requires extensive step distillation, guidance

optimization (Salimans and Ho, 2022; Song et al., 2023; Sauer et al., 2024; Yin et al., 2024b,a; Liu et al., 2023b; Fan et al., 2026; Ho and Salimans, 2022; Meng et al., 2023; Fan et al., 2025; Zhou et al., 2026), and kernel-level improvements (Dao et al., 2022; Dao, 2024; Shah et al., 2024; Ansel et al., 2024; Chen et al., 2025a; Zhu et al., 2026; Yang et al., 2025). AssetGen co-designs synthesis and acceleration: rather than texturing abstract latents, we condition a synchronized model directly on the deployable, normal-baked mesh. By combining view-selective attention with distillation and global pipeline optimizations, we achieve high-fidelity texturing within real-time deployment constraints.

Mesh Processing and Production Pipelines. To satisfy rendering constraints, asset generation relies on foundational geometry processing, including mesh simplification (Garland and Heckbert, 1997; Hoppe, 2023; Lindstrom and Turk, 1998; DeCoro and Tatarchuk, 2007), UV parameterization and seam placement (Lévy et al., 2023; Sheffer et al., 2005; Young, 2023; Xu et al., 2025), and normal baking (Cohen et al., 1998), supported by efficient GPU rendering libraries (Laine et al., 2020; Ravi et al., 2020; Pidhorskyi et al., 2024; Parker et al., 2010). Building on these primitives, complete 3D generation systems increasingly integrate geometry, texture, and export stages (Bensadoun et al., 2024; Zhao et al., 2025b; Hunyuan3D et al., 2025; Lei et al., 2025; Boss et al., 2025; Xiang et al., 2025b,a; ByteDance Seed3D Team, 2026). AssetGen contributes a complementary system perspective to this design space: rather than treating model inference, geometry processing, and texture fusion as independent modules, we co-design and globally optimize the full pipeline. This approach yields an application-ready, UV-unwrapped, and normal-baked mesh while exposing distinct latency-quality operating points for interactive deployment.

3 System Overview

AssetGen takes a single image as input and generates a textured 3D mesh optimized for real-time rendering. The system consists of three major stages: geometry generation (MeshGen), geometry processing, and texture generation (TextureGen). We illustrate this workflow in figure 2. In particular, we use an explicit geometry-first pipeline, in which MeshGen predicts a dense 3D surface that captures global shape and local structure. The geometry processing stage then converts this dense surface into a lightweight asset through simplification, hidden-face culling, UV unwrapping, and tangent-space normal baking. TextureGen renders normal and position maps from the processed asset, synthesizes multi-view color images conditioned on those maps and the reference image, and fuses the generated views into the UV atlas through visibility- and incidence-weighted backprojection, with 3D-aware inpainting for regions not observed by any view. The final output is an explicit textured mesh with a small triangle count, UV coordinates, and a diffuse texture atlas.

We expose two inference configurations with different quality vs. latency trade-offs. The default AssetGen configuration uses two-stage coarse-to-refine MeshGen, runs TextureGen at 1024px per view with inference-time CFG, and applies per-view super-resolution before atlas fusion. This configuration prioritizes visual quality and runs in approximately 30 seconds end to end when deployed on H100 GPUs. AssetGen Flash skips MeshGen refinement, runs TextureGen at 768px per view, uses a guidance-distilled conditional-only TextureGen model, omits per-view super-resolution, and exports a 1K atlas, reducing end-to-end latency to approximately 14 seconds.

Next, we describe data curation (section 4), geometry generation (section 5), geometry post-processing (section 6), texture generation (section 7), inference acceleration (section 8), evaluation (section 9), qualitative results (section 10), conclusion and limitations (section 11).

4 Data Filtering and Curation

The quality of a 3D generator depends strongly on the quality of the training data, which we enforce via rigorous curation. We started from a large collection of in-house licensed datasets, but identified issues such as duplicates, background presence, 3D scans with degenerate geometry, inconsistent orientation and low mesh quality, as shown in Fig. 3. We filtered out problematic assets using geometric rules and a Vision-Language Model (VLM).

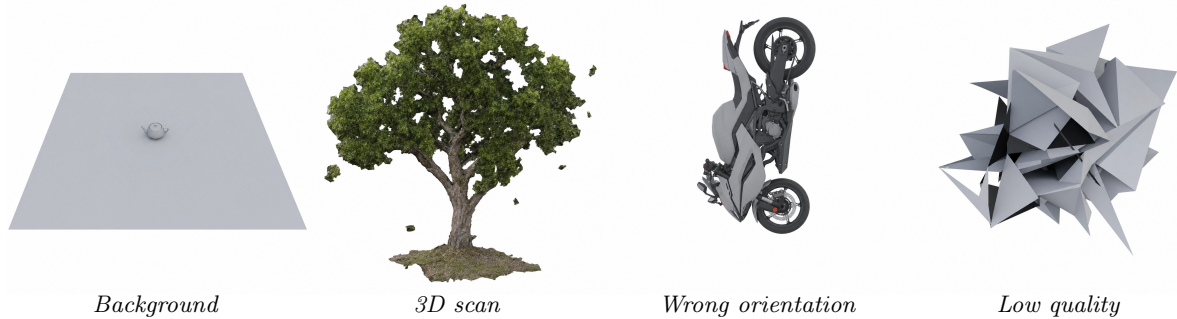


Figure 3 Examples of assets removed during semantic filtering: background geometry, 3D scans, incorrect orientation, and low mesh quality.

Geometric Filtering We started by identifying and removing *duplicates* (e.g., objects that only had minor texture or geometric differences), using metadata and vertex count to identify them and retaining only the variant with the largest file size. We also removed meshes with very low or very large polygon counts, often corresponding to placeholders or 3D scans. This filtered around 30% of the assets. Approximately 3% of the assets contained *animations*. From these, we selected the rest pose and some additional representative poses using max-distance sampling to encourage diversity.

Semantic Filtering The remaining assets underwent a multi-stage, VLM-driven semantic filtering process. Each stage targets a specific failure mode, removing roughly 30% assets in total. First, artist-created models often include *background* geometry (e.g., skydomes, ground planes, and surrounding cylinders) that interferes with object-centric generation. We employ a two-stage detection mechanism: a lightweight heuristic detector first flags candidates based on geometric properties (e.g., outlier size, detached planar components), followed by a VLM classifier to filter false positives. Second, photogrammetric *3D scans* and *satellite imagery*, which typically exhibit jagged boundaries, noisy surfaces, and non-manifold topology, are identified and removed via a dedicated VLM pass, filtering roughly 4% assets. Third, a large fraction of meshes exhibit incorrect *3D orientation*, appearing upside-down or sideways. We render four canonical views at a fixed elevation and apply an orientation predictor using majority voting to determine the 3D orientation. A VLM then verifies predictions falling outside a plausible elevation range. Objects with confirmed incorrect gravity are first removed (approximately 2%). Then, all retained meshes whose predicted frontal view deviates from the canonical forward direction are re-aligned, ensuring global orientation consistency across the training set. Finally, the VLM was used to score each asset based on *geometric fidelity* and *texture quality* (both on a 0–10 scale) and to flag visual artifacts such as rendering glitches, anomalous viewing angles, transparency errors, or residual backdrops. Assets with severe geometric degradation (score ≤ 2) or flagged artifacts were excluded. This step removed approximately 20% assets.

5 MeshGen

Given a single input image, MeshGen reconstructs the object 3D shape in the form of a mesh. This section details the training data, model architecture, and distillation strategy to accelerate inference.

5.1 MeshGen Data Preparation

MeshGen relies on signed distance functions (SDFs), which require the identification of interior and exterior volumes to be well-defined. To do so, we first convert raw 3D assets into watertight meshes.

We found standard methods employing ray tracing (Zhang et al., 2024) or winding numbers (Zhao et al., 2025b) to be unreliable; ray tracing is slow and fails near holes and slits, while winding numbers degrade with inconsistent face orientations. Therefore, we use an adaptation of the flood-fill algorithm (Smith, 1979) that is robust to these defects. We identify the exterior with voxel-grid flood filling, accelerated by a GPU Bounding Volume Hierarchy (BVH). First, we mark a narrow surface band: voxels whose unsigned distance to the input

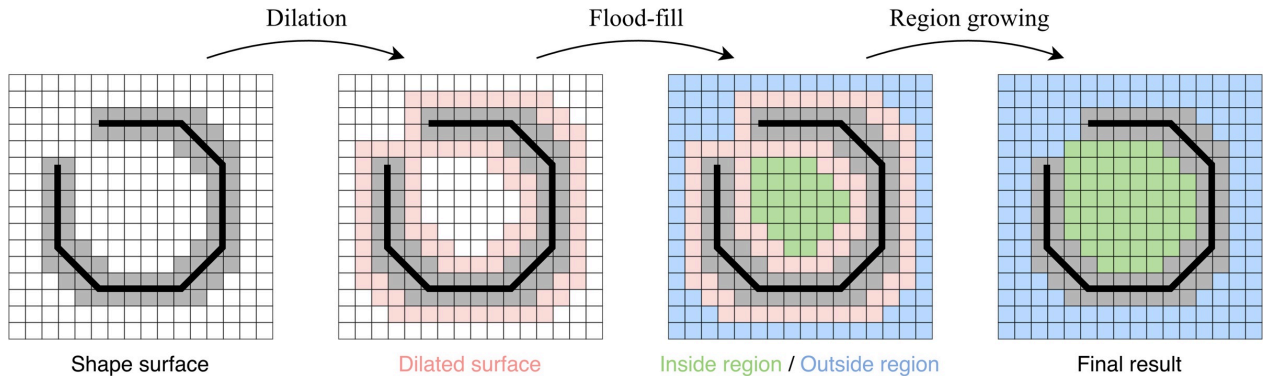


Figure 4 Overview of the flood-fill-based voxel sign estimation algorithm (shown in 2D cross-section). See the text for details.

surface is below a fixed threshold. We then flood fill from the grid boundary, stopping at this band. Small gaps in the band can cause leakage into the interior. Dilation seals these gaps but shifts the surface boundary, which cannot be compensated by erosion without removing high-frequency boundary detail.

We address this issue with a three-stage algorithm, illustrated in [figure 4](#). First, we dilate the surface band (gray) to close the gaps in the input mesh, producing an expanded band (pink). Second, we flood fill from the voxel-grid boundary: flooded voxels are exterior (blue), dry voxels are interior (green), and voxels in the dilated band remain undetermined (pink). Third, we resolve undetermined voxels by assigning the label that best agrees with their neighbors. This replaces naïve erosion, while preserving high-frequency boundary detail. Since dilation can create small artificial cavities in concave regions or between nearby parts, we identify them as small connected components from the inferred interior and return them to the unknown set before final relabeling.

After labeling, we extract a watertight mesh with marching cubes and compute SDF supervision from the resulting surface for training.

5.2 MeshGen Architecture

MeshGen generates 3D shapes from a single image using a latent diffusion transformer operating on the VecSet ([Zhang et al., 2023](#)) representation. The model employs a coarse-to-refine architecture: an initial stage establishes the rough shape and topology of the object, and a refinement stage adds higher-resolution detail.

Formulation MeshGen follows a standard conditional latent diffusion formulation over VecSet shape latents. We summarize the formulation briefly, as the main system contribution lies in converting dense 3D generation into a latency-constrained, exportable asset pipeline. Given an image \mathbf{I} , we generate a 3D shape with a diffusion transformer (DiT) ([Peebles and Xie, 2023](#)) operating in the VecSet latent space. The VecSet Variational Auto-Encoder (VAE) encodes the input shape (initially represented as a set of 3D points with normals) into a compact set of N latent tokens $\mathbf{z} \in \mathbb{R}^{N \times D}$; the decoder maps \mathbf{z} to a corresponding SDF function, which can be queried at any spatial location to recover the shape. For generation, we train a denoising model ϕ_θ to reverse a forward diffusion process that progressively corrupts a clean latent code $\mathbf{z}_0 \sim q(\mathbf{z})$ into Gaussian noise. We adopt the *v-prediction* ([Salimans and Ho, 2022](#)) parameterization with a scaled-linear beta schedule and zero-SNR rescaling ([Lin et al., 2024](#)). At each timestep t , the noisy latent $\mathbf{z}_t = \alpha_t \mathbf{z}_0 + \sigma_t \epsilon$ is constructed from the noise schedule coefficients α_t, σ_t , and the model predicts the velocity $\mathbf{v}_t = \alpha_t \epsilon - \sigma_t \mathbf{z}_0$. The training objective is $\mathcal{L}_{\text{DM}} = \mathbb{E}_{t, \epsilon, \mathbf{z}_0} [\|\phi_\theta(\mathbf{z}_t, t, \mathbf{c}) - \mathbf{v}_t\|^2]$ where \mathbf{c} denotes the image conditioning.

Classifier-free guidance (CFG) ([Ho and Salimans, 2022](#)) is used to improve sample quality. During training, the conditioning \mathbf{c} is randomly dropped with probability p_{cfg} . At inference, the guided prediction is computed as $\tilde{\mathbf{v}}_t = \mathbf{v}_t^{\text{uncond}} + s \cdot (\mathbf{v}_t^{\text{cond}} - \mathbf{v}_t^{\text{uncond}})$ where s is the guidance scale. This requires two forward passes per denoising step (conditional and unconditional), which is subsequently eliminated via progressive distillation ([section 5.3](#)).



Figure 5 Visualization of the dense meshes predicted by our two-stage coarse-to-refine MeshGen, prior to geometry processing and simplification.

Architecture The backbone follows the DiT design (Peebles and Xie, 2023) with skip connections and AdaLN modulation. It maps the noisy latent code \mathbf{z}_t to the predicted velocity $\mathbf{v}_t = \phi_\theta(\mathbf{z}_t, t, \mathbf{c})$ through an input projection, a stack of DiT blocks, and an output projection. A linear layer projects the $N \times D$ noisy latent tokens to the transformer hidden dimension D_T , where N denotes the number of latents. The input image \mathbf{I} is encoded by a frozen DINOv2 ViT-G/14 with registers (Oquab et al., 2023; Darcet et al., 2024), producing a sequence of patch tokens $\mathbf{c} \in \mathbb{R}^{L \times D_c}$ at resolution 518px. The transformer uses n blocks, each consisting of three sub-layers with residual connections: (i) self-attention among latent tokens with AdaLN and query-key normalization, (ii) cross-attention to the image condition tokens \mathbf{c} with AdaLN, and (iii) a SwiGLU feed-forward network (Shazeer, 2020) with gated activation. The final token representations are layer-normalized and linearly projected back to $N \times D$, predicting the velocity \mathbf{v}_t .

Our DiT is a 2.3B parameter model, it uses $n = 24$ blocks with hidden dimension $D_T = 2048$, 16 attention heads and skip connecting the first/last 11 blocks. The latent code at this coarse stage uses $N = 4096$ tokens of dimension $D = 64$.

Implementation details For training stability and efficiency, we train our model in three stages by gradually increasing the number of latent tokens N from 512 to 4096. In the first stage, we use $N = 512$ tokens and train for 750K iterations with a learning rate of 1×10^{-4} and a batch size of 2048 samples. In the second stage, we use $N = 2048$ and train for 500K iterations with a learning rate of 2×10^{-5} and a batch size of 1280. In the third stage, we use $N = 4096$ and train for 250K iterations with a learning rate of 1×10^{-5} and a batch size of 1024. For all stages, similar to the VAE training, we use AdamW (Loshchilov and Hutter, 2017), a weight decay of 0.01, $\beta = (0.9, 0.95)$, and bfloat16 mixed precision.

Coarse-to-refine generation A single-stage model with $N = 4096$ latent tokens captures the overall shape but often lacks the resolution needed for fine geometric detail. We recover them by introducing a second stage inspired by LATTICE (Lai et al., 2025a).

The refinement model takes the coarse mesh as input and predicts a higher-resolution latent code with $N_{\text{refine}} = 16,384$ tokens. To construct the refinement tokens, we sample surface points from the coarse mesh and voxelize them to produce N_{refine} 3D positions $\mathbf{x}_i \in \mathbb{R}^3$ for each latent token. These positions serve as

RoPE input in the refinement transformer’s self-attention layers, anchoring each latent token to a specific location on the coarse geometry. This is different from the coarse stage, where tokens have no preferential spatial association *a priori*, and allows the model to focus more easily on local details rather than the global structure.

The refinement stage also uses higher-resolution image conditioning: the DINOv2 encoder operates at 1022px resolution, producing $4\times$ more patch tokens than in the coarse stage. The predicted refined latent code is decoded through a dedicated refinement VAE trained with point jittering to make it robust to voxelization. The decoder shares the coarse VAE interface—querying an implicit field and extracting the final surface via marching cubes—but uses the denser, spatially anchored token set to recover local surface detail around the coarse prediction. Because the refinement stage is guided by the coarse geometry rather than solving global structure from scratch, it converges in fewer diffusion steps.

5.3 MeshGen Distillation

At inference, the default MeshGen configuration uses 100 denoising steps for the coarse stage and 20 steps for the refinement stage, both with CFG, which further doubles the number of forward passes of the DiT. We distill both models to accelerate inference while preserving quality.

We apply progressive distillation (Salimans and Ho, 2022) to each stage, reducing iterations from 100 to 25 and from 20 to 5 respectively (a $4\times$ reduction in denoising steps). We also fold CFG into the distilled model to reduce compute and maximize speed: during training, the teacher uses guided sampling, and the student learns to reproduce the guided output in a single conditional forward pass. To train the student, we use a DDIM-based target-inversion objective. At each training step, the teacher starts from a randomly sampled student timestep and runs N deterministic DDIM steps to produce a multi-step target. The student is trained with an MSE loss to match this multi-step teacher output in a single step, using an inverted v -prediction target. Optionally, we add an auxiliary x_0 reconstruction loss that penalizes deviation between the student’s predicted clean latent and the ground truth, providing light regularization without changing the primary distillation objective.

Overall, on a single NVIDIA A100 80GB GPU, distillation reduces latency from 13.9 to 1.9 seconds for the coarse stage, and from 14.3 to 1.9 seconds for the refinement stage. To validate the distillation quality, we use human evaluation as well as quantitative metrics such as Chamfer distance do not sufficiently capture perceptual fidelity. We curate 200 teacher-student output pairs spanning diverse categories (objects, characters, and environmental elements) and representative image-to-3D benchmark inputs, and present them in a randomized, blind side-by-side comparison. As summarized in table 1, evaluators prefer the teacher in 32.9% of comparisons, the student in 30.5%, and judge 36.6% as similar, suggesting that a $4\times$ reduction in sampling steps incurs negligible perceptible quality loss. See figure 5 for example MeshGen meshes.

Table 1 Human evaluation of quality across 200 pairs (1018 total votes). The $4\times$ -distilled student closely matches the teacher in perceptual quality. Latency is measured on A100 GPU.

Model	Steps	Sec./sample	Wins	Similar	Win Rate
Teacher	120	28.20	335	373	32.9%
Student	30	3.78	310	373	30.5%

6 Geometry Post-Processing for Runtime Assets

The output of MeshGen is an SDF, from which we extract an explicit surface mesh. We first run marching cubes at a high resolution (512^3) to obtain a dense mesh with roughly one million faces. This dense extraction preserves the high-frequency geometry and serves as the source geometry for subsequent processing. However, it is not directly suitable as a deployable asset: it is too dense for real-time rendering, may contain hidden interior surfaces, and does not provide the UV parameterization required for texture mapping. We therefore convert it into a texture-ready asset through mesh simplification, visibility pruning, UV unwrapping, and

Table 2 Mesh simplification performance on 200 benchmark assets at 5K and 10K face targets. We evaluate geometric deviation (Chamfer, Hausdorff), orientation consistency (Flipped Normals across 24 views), and the mean angular error of both baked and unbaked geometric normals (Baked Mean, Geo Mean). All metrics are averaged over the benchmark (\downarrow lower is better).

Target	Method	Latency (s)	Chamfer ($\times 10^{-5}$) \downarrow	Hausdorff ($\times 10^{-3}$) \downarrow	Flipped Normals \downarrow	Baked Mean ($^\circ$) \downarrow	Geo Mean ($^\circ$) \downarrow
5k	Houdini	14.64	36.5	5.19	3956	9.02	12.39
	CuMesh (original)	0.437	29.6	6.57	1593	10.58	14.94
	CuMesh (ours)	0.469	13.3	4.59	1126	9.39	11.94
10k	Houdini	11.58	29.7	3.87	997	6.60	9.39
	CuMesh (original)	0.429	8.70	1.90	454	7.02	10.78
	CuMesh (ours)	0.457	3.01	0.97	268	6.47	8.66

tangent-space normal baking. The normal map transfers high-frequency surface detail from the dense source mesh onto the simplified mesh, yielding a compact representation suitable for real-time rendering on mobile.

6.1 Mesh Simplification

We considered using production-grade mesh simplification software, but found existing solutions too slow for our purposes. We therefore develop our own solution.

We build on CuMesh*, a library that implements parallel edge collapse with quadric error metrics (QEM) (Garland and Heckbert, 1997; Oh et al., 2025) that runs in less than one second on a GPU for our target mesh size. The algorithm maintains a quadric Q_v for each vertex v , encoding the squared distance $E(\mathbf{v}) = [\mathbf{v}; 1]^\top Q_v [\mathbf{v}; 1]$ of a point \mathbf{v} to all incident face planes. The cost $\min_v E(\mathbf{v})$ of collapsing an edge (v_0, v_1) is computed from the combination $Q = Q_{v_0} + Q_{v_1}$ of the quadrics of its two endpoints.

The baseline CuMesh implementation does not solve for the QEM-optimal position; it uses Q only to rank candidate collapses, then places the contracted vertex at the midpoint (interior edges) or an endpoint (boundary edges). This means the collapse ordering reflects the QEM objective, but the actual vertex positions do not, leading to systematic geometric degradation under aggressive polygon reduction. We compute the contraction position from the merged quadric directly, with an edge-constrained projection for stability. For interior edges, we compute the unconstrained QEM minimizer \mathbf{v}_{opt} of the energy $E(\mathbf{v})$.[†] We then project \mathbf{v}_{opt} onto the edge segment $\mathbf{v}(t) = (1-t)\mathbf{v}_0 + t\mathbf{v}_1$ by computing $t = \langle \mathbf{v}_{\text{opt}} - \mathbf{v}_0, \mathbf{v}_1 - \mathbf{v}_0 \rangle / \|\mathbf{v}_1 - \mathbf{v}_0\|^2$ and clamping $t \in [0, 1]$. This bounds vertex displacement to the edge length while following the QEM objective. When the quadric is singular, we fall back to the midpoint. For boundary edges, we keep boundary vertices fixed or select the lower-error endpoint. The same placement logic is used for both cost evaluation and actual collapse, ensuring the ordering reflects the true geometric cost.

Mesh simplification results We evaluate the impact of optimal placement on a benchmark of 200 meshes generated by our image-to-3D pipeline, comparing three configurations: Houdini’s PolyReduce as a representative production-quality CPU solver, CuMesh with the baseline midpoint placement (original), and CuMesh with our optimal placement strategy (ours). Each mesh is simplified to two target face counts (5k and 10k) and compared against the raw mesh.

We measure the following metrics: The *Chamfer distance* samples 256k surface points from the original and simplified meshes and reports the average minimum distance of points in one set against the other, in both directions. The *Hausdorff distance* does the same but reports the maximum minimum distance. The *Flipped normal* metric renders the simplified mesh from 24 viewpoints with and without backface culling at resolution of 1024 and reports the number of pixels where the two renderings disagree, caused by a flipped normal. *Baked mean* bakes the normals from the original mesh to the simplified one and reports the average angular error in degrees of the approximation.[‡] *Geo mean* reports the average angular error between the simplified

*<https://github.com/visualbruno/CuMesh>

[†]I.e., we solve $A\mathbf{x} = -\mathbf{b}$ (where A is the upper-left 3×3 block of Q and \mathbf{b} its upper-right 3×1 column).

[‡]The simplified mesh is UV-unwrapped via xatlas, and a normal map is baked from the raw mesh onto the simplified mesh’s UV layout. Surface points are then sampled uniformly on the simplified mesh, and the angular error between the baked normal and the true raw-mesh normal is computed at each sample. The metric reports the mean error in degrees across all samples.

and original mesh true normals.

Results are summarized in [table 2](#). The optimized placement improves over the CuMesh baseline across all metrics. Compared with Houdini, the optimized CuMesh achieves better geometric fidelity on most measures—Chamfer distance, Hausdorff distance, flipped normals, and geometric-normal error—with Houdini slightly ahead only on baked-normal error at the 5k-face target.

6.2 Hidden Face Removal

Generated meshes can contain interior faces that are invisible from any exterior viewpoint. Such faces waste polygon and texture budget, complicate UV unwrapping, and may create downstream artifacts in rendering or rigging. We remove them with a GPU-accelerated visibility pass followed by topology-aware cleanup.

The visibility pass builds a BVH over the mesh and casts rays from 512 viewpoints distributed on a surrounding sphere at 1024-pixel resolution. A face is marked visible if at least one ray reaches it without occlusion. The BVH is constructed once and reused across all viewpoints, and the result is accumulated directly into a per-face visibility mask.

Pure visibility classification produces fragile results under self-occlusion: rays can miss faces that belong to the exterior surface but are shadowed by other geometry, leaving isolated floating triangles or holes in the visible shell. A topology-aware flood-fill step addresses this by propagating exterior classification across the mesh’s connectivity. The flood fill is seeded from faces already classified as visible by ray tracing. Propagation proceeds via breadth-first traversal across edges, gated by a normal consistency check: an adjacent face is promoted to exterior only if its normal agrees in direction with the seed face, preserving winding consistency and preventing propagation through the interior.

Results We evaluate the pipeline on 100 meshes produced by our generation model, each containing approximately 22K faces after simplification. The core hidden-face-removal kernel runs in 0.179 seconds per mesh on average on a single GPU. In the production pipeline, the corresponding stage averages 0.362 seconds once staging and scheduling overhead are included.

6.3 UV Unwrapping

After simplification and hidden face removal, we construct a UV atlas for the mesh to support normal baking and texturing in subsequent stages. We use xatlas [§] for UV unwrapping. It operates in three stages: chart segmentation, which partitions the mesh surface into regions suitable for planar mapping; LSCM-based parameterization, which computes low-distortion 2D coordinates for each chart; and atlas packing, which arranges charts into a texture atlas.

Of these, chart segmentation dominates runtime because it grows charts one face at a time with a greedy priority queue over normal-compatibility costs, serially. We first evaluated CuMesh’s GPU-based chart segmentation [¶], which uses parallel edge collapse with normal-cone merging. However, this rebuilds the graph after each round of edge collapse, causing frequent synchronization across small GPU kernels and leads to no acceleration for meshes with fewer than 30k faces as the kernel launches become the bottleneck.

We instead introduce a parallel chart segmentation pipeline that partitions the mesh spatially, runs segmentation on each partition with boundary overlap, and reconciles the results through a merge pass. The approach follows a four-phase partition-with-overlap strategy. First, we recursively bisect the mesh into spatially balanced regions using median-area splits along the axis of maximum centroid spread, producing a set of compact macro-partitions. Second, we extract an N-ring halo of neighboring faces around each partition boundary via breadth-first traversal, so that each partition’s segmentation has geometric context about adjacent regions and does not produce arbitrary chart boundaries at partition edges. Third, we run the full xatlas segmentation pipeline independently on each partition (core faces plus halo) in parallel using the existing task scheduler. Fourth, we reconcile the per-partition results into a unified chart assignment through a three-step boundary reconciliation: core faces are assigned to charts from their owning partition, orphan faces (those in halo zones

[§]<https://github.com/jpcy/xatlas>

[¶]<https://github.com/visualbruno/CuMesh>

that were not claimed) are assigned to the neighboring chart with the best normal compatibility, and a final pairwise merge pass—ported from *xatlas*’s serial merge logic with the same five merge criteria (single-face absorption, quad absorption, enclosed chart, significant shared boundary, and normal gate)—consolidates fragmented charts at partition boundaries while validating that merged normals remain coherent.

Human Evaluation We conducted a human evaluation of final texture quality, where the only variable between conditions is the UV unwrapping algorithm—all other pipeline stages (mesh generation, simplification, and texture synthesis) are held constant. Across two evaluation rounds totaling 604 pairwise comparisons, the combined results are summarized in [table 3](#). The serial baseline holds a marginal advantage at 51.9% win rate, while the parallel unwrap provides a $1.9\times$ speedup on average. Annotators reported that distinguishing the two methods required zooming in to inspect seam boundaries, and that the differences were not visible on mobile devices. This makes UV parameterization a good Pareto trade: a visible latency reduction with no practically observable degradation for interactive use.

Table 3 Human evaluation of UV unwrapping quality comparing serial and parallel *xatlas* across 604 pairwise comparisons. Processing speed is normalized to the serial baseline.

Xatlas	Speed (s)	Wins	Losses	Ties	Total	Win
Serial	4.70	241	217	146	604	51.9%
Parallel	2.56	217	241	146	604	48.1%

6.4 Normal Map Baking

The simplification stage retains the raw high-poly mesh alongside the simplified output. We bake a tangent-space normal map that transfers high-poly surface detail onto the simplified mesh’s UV layout, recovering geometric fidelity that would otherwise be lost to polygon reduction.

Blender’s Cycles renderer produces high-quality normal maps but averages 2.92s per mesh in our benchmark and can take up to 25.85s in the worst case. It also incurs data-conversion overhead: the mesh must be exported for Blender to load, and the baked output must be saved and read back, adding further latency. We replace Blender with a GPU-resident pipeline that keeps all data in memory, eliminating inter-process overhead. The pipeline has four stages.

The pipeline rasterizes the low-poly mesh into its own UV space using DRTK ([Pidhorskyi et al., 2024](#))^{||}, producing a G-buffer with world-space position, smooth normal, tangent, and bitangent for each valid texel. A GPU BVH built on the high-poly mesh then locates, for each texel’s world-space position, the closest point on the high-poly surface and retrieves its interpolated smooth normal via barycentric weighting. Two filters reject erroneous correspondences: a distance filter discards hits beyond 1% of the bounding-box diagonal, and a UV-reliability filter marks texels on faces with degenerate UV parameterization as unreliable, assigning them a neutral tangent-space normal $(0, 0, 1)$. The hit normal is projected into the texel’s tangent frame, encoded as RGB8, and dilated at UV seam boundaries to prevent mipmap bleed. The entire pipeline runs on the GPU with no disk I/O.

Table 4 Comparison of normal baking performance between our GPU-resident implementation and Blender. Evaluated across 50 benchmark assets at a target of 5K faces and 1024×1024 texture resolution.

Metric	Method	Mean	Median	Max
Bake latency (ms)	Blender	2,920	1,842	25,854
	GPU	271	188	1,147
Baked mean ($^{\circ}$)	Blender	9.89	6.98	54.39
	GPU	9.66	7.14	50.35

^{||} <https://github.com/facebookresearch/DRTK>

Evaluation. We evaluate normal baking on 50 meshes, each simplified to 5k faces and paired with a raw high-poly source, as shown in Table 4. All methods use xatlas UVs and 1024×1024 tangent-space normal maps. Our GPU baker achieves comparable quality to Blender while substantially reducing latency. It runs $10.8\times$ faster on average (271 ms vs. 2,920 ms) and $22.5\times$ faster in the worst case (1,147 ms vs. 25,854 ms). The mean angular error is slightly lower than Blender (9.66° vs. 9.89°), while Blender has a small median advantage (6.98° vs. 7.14°).

7 TextureGen

The geometry stage outputs a simplified mesh, a UV atlas, and a tangent-space normal map that transfers high-frequency detail from the dense source. The next step is TextureGen, which generates a UV texture for the object.

TextureGen decomposes the problem into two stages: image-space appearance synthesis and UV-space geometric fusion. First, a multi-view diffusion transformer generates a coherent set of textured views conditioned on rendered geometry, the reference image, and text. Second, a projection module fuses these views into the UV atlas and completes unobserved regions. This separation leverages strong image-space diffusion priors while keeping the final texture geometrically aligned to the mesh, following recent work (Bensadoun et al., 2024; Cheng et al., 2025). For interactive production use, we combine multimodal conditioning with efficient multi-view attention (Section 7.2), progressive distillation from a 32-step teacher to 4 steps (Section 7.3), and fast UV backprojection and completion (Section 7.4). See figure 8 for example TextureGen results.

7.1 TextureGen Data Preparation

The TextureGen generator takes as input the 3D mesh and several target viewpoints, encoded as set of normal and position map renders, along with a reference image capturing the object appearance, and text prompt describing the object. It generates as output several images of the textured object, one for each target view. We explain below how the training data is obtained from each 3D asset.

Images. To obtain the *reference image*, we render the 3D assets from a random camera viewpoint with azimuth and elevation in the range -45° to 45° sampled in five discrete increments. For each viewpoint, we render the mesh in two variants, one illuminated by a randomly selected and oriented HDRI image from a set of HDRI images with varying degrees of directional strengths, and one by a relatively diffuse HDRI image. This makes the model robust to passing reference images that range from harsh directional lighting to flat diffuse appearance.

To obtain the *target images*, we render the 3D asset from ten fixed viewpoints: 8 side views at 45° azimuth increments, along with top and bottom views. We use orthographic projection because it decouples projection scale from depth, yielding predictable foreground coverage for normalized assets. It also gives side views a shared vertical coordinate: pixels in the same image row correspond to the same 3D height, which simplifies learning cross-view consistency.

We scale the mesh to fit in a fixed sphere and render world-space normals and positions for each view. We apply normal maps that come with the asset so the conditioning signal retains micro-surface details. Position maps store the visible 3D coordinate at each pixel.

We task TextureGen with generating a color texture (instead of PBR materials) as this is more friendly with runtime rendering on mobile devices. We thus optimize the color targets to be visually appealing and informative, including soft shadows, ambient occlusion, and surface gradients, while avoiding view-dependent effects, such as specular reflections, that cannot be represented by a color texture.

Rendering the asset using a softly-lit environment is visually appealing, but results in view-dependent effects. Those are removed by using diffuse illumination, but the latter results in a flat appearance that does not capture well the object shape and material. We thus randomly blend these two renders, where the same weights are used across all 10 views and are sampled in the range from 0.2 (i.e., 20% diffuse image) to 0.5 for each training step.

Text Prompts We use a Vision-Language Model (VLM) to caption the asset and obtain a corresponding text prompt. To do so, we compose four renders into a 2×2 grid and feed it to the VLM, prompting it to describe the object as a whole. Then, we flag poor descriptions that contain refusals, prompt echoes, meta-references, or insufficient content and ask an LLM to rewrite those preserving only factual object descriptions. Finally, we task the LLM with summarising captions to a length of at most 128 tokens.

7.2 TextureGen Architecture

The core of TextureGen is a multi-view diffusion transformer that synthesizes a coherent set of color images from a reference image, text prompt, and per-view geometric renderings. Let $\mathbf{I} \in \mathbb{R}^{H \times W \times 3}$ denote the reference image, \mathcal{M} the processed mesh, and $\{\mathbf{N}_k, \mathbf{P}_k\}_{k=1}^K$ the normal and position maps rendered from K views. Given these inputs, the model generates textured views $\{\mathbf{V}_k\}_{k=1}^K$ simultaneously. We describe its latent formulation, conditioning design, and structured multi-view attention.

Formulation. TextureGen operates in the latent space of a pretrained image VAE. Each 1024×1024 view is encoded as a 64×64 latent. The reference image and the K target views are arranged into a $1 \times (1+K)$ latent grid: the first slot contains the reference image, and the rest are reserved for noisy target-view latents. The latent in the reference slot is pinned throughout denoising, so the model treats it as a fixed appearance anchor. The training loss is applied only to the K target-view slots.

We train the model with optimal-transport conditional flow matching (Tong et al., 2023; Kornilov et al., 2024) and a uniform timestep schedule. The model predicts a velocity field $\mathbf{v}_\theta(\mathbf{z}_t, t, \mathbf{c})$, where \mathbf{z}_t is the noisy multi-view latent at time t and \mathbf{c} collects the geometric renders, pinned reference image, and text conditioning.

Architecture. The backbone is a diffusion transformer with 30 layers, hidden dimension 3072, 24 attention heads, and SwiGLU feed-forward layers with $4\times$ expansion. Each block applies AdaLN-Zero modulation from the diffusion timestep, followed by self-attention, cross-attention to text embeddings, and a feed-forward layer. The transformer processes the reference and target-view latents jointly, allowing appearance cues from the reference slot and geometric cues from each target view to interact during denoising.

For each target viewpoint, the rendered normal map \mathbf{N}_k and position map \mathbf{P}_k are encoded at the latent resolution and concatenated with the noisy target-view latent along the channel dimension. This provides dense geometric context: surface orientation from normals and surface correspondence from world-space positions.

The pinned reference slot provides the main appearance signal, including color, material, and style. Because it is part of the same latent grid as the generated views, the model can propagate reference appearance through self-attention. For CFG, the unconditional branch replaces the reference image with a uniform-white latent, allowing the guidance scale to control adherence to the visual reference.

Text prompts provide complementary semantic information that may be ambiguous from the reference image alone. Text embeddings from T5 and CLIP are injected through cross-attention in each transformer block.

Structured multi-view attention. Full self-attention over $(1+K)$ latent slots is expensive when $K=10$ and each slot contains 64×64 tokens. Instead, we use a sparse attention pattern matched to the camera layout. Each target view attends to the reference slot and a small set of adjacent views. Cardinal side views attend to the reference and their two neighboring views; diagonal views attend to the reference and neighboring cardinal views; top and bottom views attend to the reference and all four cardinal views. Learned per-slot positional offsets identify each view within the grid.

For $K=10$, full attention would involve 45,056 tokens across the reference and target views. The structured pattern reduces the per-view attention context by roughly $4\times$ while preserving the connections needed for cross-view consistency: every view sees the reference image, and neighboring views share overlapping surface regions.

7.3 TextureGen Distillation

Similarly to Section 5.3, we use progressive distillation Salimans and Ho (2022) for TextureGen that progressively reduces denoising steps $32 \rightarrow 16 \rightarrow 8 \rightarrow 4$. We apply this to two model configurations: the default, AssetGen, uses a 4-step sampler (with CFG during sampling) to produce highest-fidelity textures at 1024×1024 resolution. AssetGen Flash takes an extra stage to fold CFG into the distilled model to generate per-view at 768×768 resolution.

Progressive Distillation. The training objective combines velocity matching with an auxiliary denoised-image prediction loss. After each stage, we select the best student checkpoint using pixel-level fidelity metrics, including PSNR and SSIM, against the immediate teacher on a benchmark suite.

CFG Distillation. Following the same protocol as progressive distillation above, we select the best student checkpoint via PSNR against the 4-step CFG teacher. We find that CFG distillation is particularly sensitive to the loss function. The baseline MSE loss establishes 30.93 dB. Switching to a Pseudo-Huber loss leads to a +1.08 dB improvement. Adding channel-wise statistics matching and timestep importance sampling reduces color drift and stabilizes early training, though it does not improve PSNR. Combining these with dynamic thresholding and a guidance-scale curriculum gives a further +0.13 dB, reaching 32.14 dB.

7.4 TextureGen Postprocessing

Given the K texture views generated by TextureGen, the next step is to transfer them onto a single UV texture map via backprojection and blending followed by inpainting to fill unobserved regions.

Backprojection We first project the K generated views to the texture UV atlas using *backward* projection**. We consider each texel in the atlas, recover its corresponding 3D surface position and project that point into each of the K generated views, reading off the corresponding color.

Pixels near object boundaries or depth discontinuities are often unreliable, since small projection errors can sample background colors or colors from the wrong surface. We therefore compute an edge mask by detecting large differences between neighboring pixels in the point coordinate maps, excluding them from backprojection.

A single bilinear sample per texel can undersample the generated view, especially at grazing angles and near UV seams where the UV-to-image mapping is highly anisotropic. We address this issue by using per-texel anisotropic filtering. For each atlas texel, we estimate its image-space footprint using finite-difference Jacobians of the UV-to-image mapping. An SVD of this footprint gives the major and minor axes: the minor axis selects the mip level, while the major axis defines a multi-sampling direction with up to 8 taps. The mip chain is built using a Lanczos-2 downsampler. We apply a small negative LOD bias (-0.5), per-level sharpening, trilinear blending between adjacent mip levels, and anisotropy-aware mip compensation to retain detail along elongated footprints.

Blending. At this point, each texel has zero, one, or more candidate colors from the K backprojected views. For each texel with at least one candidate, we blend the contributions using an incidence-weighted scheme.

For each view k , we compute an incidence map $I_k \in [0, 1]^{H_{uv} \times W_{uv}}$ in UV space. Each texel is assigned a reliability score based on its surface orientation and visibility from the camera. The raw incidence is the clamped dot product between the surface normal \mathbf{n} and the viewing direction \mathbf{d}_k : $I_k^{\text{raw}} = \max(0, \mathbf{n} \cdot \mathbf{d}_k)$. We then apply a depth-buffer visibility test. The texel’s 3D position is projected into view k , and its projected depth is compared against the rasterized depth buffer. If the texel is occluded beyond a fixed tolerance, its incidence is set to zero. Thus, I_k is nonzero only for texels that are both front-facing and visible in view k .

Backprojecting view k produces a partial atlas A_k . We blend the partial atlases using the incidence maps and a per-view prior: $T = \sum_{k=1}^K w_k I_k^\alpha \odot A_k / (\sum_{k=1}^K w_k I_k^\alpha + \epsilon)$, where α controls the sharpness of the blend and w_k encodes a view prior. We assign higher weights to perceptually important views: $w_k = 1$ for the front and rear views, 0.3 for top and bottom, 0.1 for the $\pm 45^\circ$ frontal side views, 0.01 for left and right side views, and 0.001 for the $\pm 45^\circ$ rear side views. Together, the incidence term and view prior favor visible, near-orthogonal observations from salient viewpoints while suppressing grazing and less informative

**Forward projection tends to leave holes and be inaccurate, particularly for grazing angles.

contributions. We implement the reduction in log space using `logsumexp` for numerical stability when α is large.

Inpainting Texels that are not reliably observed from any generated view remain unfilled after blending.

Following MVPaint (Cheng et al., 2025), we use the 3D geometry to guide texture completion in UV space. Given the blended atlas, a binary missing-region mask, and per-texel position and normal maps, we build a KD-tree over known texels in 3D position space. For each unknown texel, nearest-neighbor candidates are retrieved in 3D and weighted by spatial proximity and normal alignment. Colors are then propagated from known to unknown texels using these geometry-aware affinities. This step fills in occluded regions using texels that are nearby on the object surface, rather than merely nearby in UV space.

7.5 Geometric Condition Rendering

One large remaining latency source for TextureGen is multi-view geometric condition rendering. During training, we use Blender to render both geometric conditions and color targets from a shared scene setup. However, Blender takes approximately 5s to render 10 views. At inference, we replace Blender with DRTK (Pidhorskyi et al., 2024), a GPU-accelerated rasterizer that renders all 10 views directly as GPU-resident tensors in approximately 500ms. In a blind evaluation, these two rendering methods produce no visible difference in the final generated textures; DRTK-based results are preferred 54.3% of the time over Blender-based results on 100 pairs.

8 Latency Optimization

We have explained how distillation reduces the cost of sampling geometry and texture, but many other factors determine end-to-end latency: surface extraction, simplification, hidden-face removal, UV parameterization, normal baking, multi-view condition rendering, backprojection, inpainting, asset serialization, and I/O. These stages stress different parts of the system: diffusion sampling saturates GPU tensor cores; geometry and texture preparation mix GPU kernels with CPU-side scheduling, KD-tree construction, and UV bookkeeping; and input download, output upload, image encoding, and asset serialization are I/O-bound.

We therefore optimize the system at two levels.

First, kernel- and precision-level optimizations reduce the cost of individual model inferences (section 8.1). Second, pipeline-level scheduling overlaps independent CPU, GPU, and I/O work so that request latency is closer to the critical path than to the sum of all stages (section 8.2). With these optimizations, AssetGen runs in approximately 30 seconds end to end, and AssetGen Flash in 14 seconds end to end (tables 5 and 6).

8.1 Kernel and Precision Optimization

We apply three optimizations to reduce latency. First, FlashAttention 3 (Shah et al., 2024) is used in both diffusion transformers, reducing latency by 20% with no observed quality change. Second, non-blocking host-to-device transfers overlap data copies with kernel execution, saving an additional 11%. Third, default-mode graph compilation (Ansel et al., 2024) is applied to the diffusion transformers and backprojection kernels, fusing element-wise operations and reducing kernel-launch overhead.

We also reduce numerical precision where possible, applying FP8 and INT8 quantization in both diffusion transformers, with precision assignments determined by sensitivity analysis. For TextureGen, embedding layers, the first and last transformer blocks, and output projections remain in higher precision, as these components are visibly sensitive to quantization.

8.2 Pipeline Optimization

We can hide most of the latency of other steps by running them in parallel. We parallelize independent work within a request.

Table 5 Latency breakdown of the MeshGen and geometry processing stages for AssetGen and AssetGen Flash. Values are averaged over 100 benchmark images. A dash (–) indicates a stage skipped by the Flash configuration. Row values represent individual stage runtimes; *the reported total reflects the measured critical-path latency rather than an arithmetic sum.*

Module	AssetGen (s)	Flash (s)
Preprocess	0.227	0.227
Coarse conditioning	0.044	0.044
Coarse diffusion	1.193	1.193
Coarse mesh decoding	1.414	1.414
Coarse surface sampling	0.636	—
Refine conditioning	0.054	—
Refine diffusion	1.671	—
Refine mesh decoding	1.704	—
Floater removal + simplification	0.654	0.654
Hidden-face removal	0.362	0.362
UV unwrapping	2.561	2.561
Tangent normal baking	0.265	0.265
Total MeshGen + geometry critical path	10.829	6.768

Table 6 Latency breakdown of the TextureGen stage. Values are averaged over 100 benchmark images. The default AssetGen configuration uses 1024px diffusion with inference-time CFG (split across two GPUs), per-view super-resolution, and a 2K texture atlas. AssetGen Flash uses 768px diffusion with a guidance-distilled conditional-only model, omits super-resolution, and exports a 1K atlas. Row values represent individual stage runtimes, while *the reported total reflects the measured critical-path latency rather than an arithmetic sum.*

Module	AssetGen (s)	AssetGen Flash (s)
Preprocess	0.346	0.228
Render conditions	0.642	0.394
Diffusion	10.455	4.420
Precompute backproject data	1.455	0.570
Build KD tree	0.908	0.274
Per-view super-resolution	3.112	—
Backprojection and inpainting	0.801	0.246
Export textured mesh	0.845	0.325
Total TextureGen critical path	18.01	6.62

Within each stage, we identify operations that have no data or resource dependency and schedule them concurrently. In TextureGen, several expensive preprocessing tasks depend only on the processed mesh and camera layout, not on the generated colors. These include UV-to-image sampling maps, visibility and incidence masks, anisotropic filter parameters, and KD-tree neighbor structures for inpainting. Because the processed mesh is fixed before texture diffusion begins, these geometry-dependent computations run in a separate worker process while diffusion sampling runs on the GPU.

Irreducible dependencies increase latency. In our design, TextureGen needs to wait for mesh simplification and normal baking to be complete, adding to the critical path.

MeshGen and TextureGen are implemented as separate services. MeshGen runs on one H100 GPU and writes the simplified mesh, UV layout, baked normal map, and associated metadata to shared storage, which is read by TextureGen to generate the texture map. For AssetGen, TextureGen uses two H100 GPUs to split the conditional and unconditional CFG branches, whereas AssetGen Flash uses only one as CFG is distilled. The data transfer cost adds roughly 1–2 seconds compared to an ideal in-process handoff, and this overhead is included in the reported results.

8.3 Latency Results

We report latency in three ways. First, [tables 5](#) and [6](#) break down the major MeshGen, geometry processing, and TextureGen stages. These values are averaged over 100 benchmark images and are intended to show where time is spent in the system. These timings should not be summed to obtain the total system latency as many of these steps run in parallel. Conversely, these timings do not account for the cost of synchronization, tensor handoff, worker scheduling, service-to-service transfer, and serialization overheads that are not always assigned to a single row. The “Total” rows report measured module-level critical-path latency (not the numerical sum of the rows), while the final end-to-end numbers are measured directly from input image to exported asset.

Second, [table 7](#) reports the time required to serve a user request end-to-end, including an additional 0.65 seconds required to segment out the object in the user-provided image. These numbers account for details of our hosted infrastructure and therefore should be interpreted as representative user-visible latency, not as a hardware-normalized benchmark.

Table 7 End-to-end wall-clock latency comparison. AssetGen measurements capture the complete pipeline from input image to exported textured mesh, averaged across 100 benchmark assets, and include a shared 0.65s image-segmentation stage. Baseline latencies reflect the time from web submission to result availability averaged over five trials, excluding export and download overhead. Because these baselines operate on unknown hosted infrastructure, the values serve as operational latency references rather than hardware-normalized benchmarks.

Method	AssetGen	AssetGen Flash	Commercial Model A	Commercial Model B	Commercial Model C	Commercial Model D
Wall-clock latency	~30s	~14s	~180s	~125s	~100s	~130s

For AssetGen, latency is measured from input image to exported textured mesh and includes image segmentation, service orchestration, serialization, and asset export. For commercial baselines, we measure website wall-clock time over five generations, from submitting the image to the point where the generated result becomes available in the web interface; we do not include additional export or download time. Because these systems run on unknown hosted infrastructure and may include website-side scheduling or queueing, these measurements should be interpreted as operational latency references rather than controlled hardware-normalized comparisons. In our measurements, hosted high-quality image-to-3D systems operate around the near-minute to two-minute regime, while AssetGen achieves similar quality in just 30 seconds, and AssetGen Flash generates a preview in less than 15.

Third, [table 8](#) provides a ladder analysis of our acceleration techniques. Unlike [tables 5](#) and [6](#), which average timings over 100 benchmark images, here we evaluate variants of the system on one fixed input and measure the cumulative effects of the optimizations. For MeshGen, replacing CPU-bound geometry processing and then applying progressive distillation, Flash Attention 3, graph compilation, I/O overlap, parallel UV segmentation, and DRTK normal baking reduces the fixed-sample latency from 103.15s to 12.25s. For TextureGen, progressive distillation provides the largest single reduction, while kernel optimizations, precomputed backprojection data, rendering optimizations, and the two-GPU CFG branch split further reduce the default quality path.

9 Evaluation

This section evaluates the quality of the assets produced by AssetGen against leading image-to-3D generators. We introduce two benchmarks assessing generation quality for general objects ([section 9.1](#)) and for characters ([section 9.2](#)), respectively. We further conduct blind human evaluation in [section 9.3](#).

Baselines. We compare AssetGen and AssetGen Flash against Commercial Model A, Commercial Model B, Commercial Model C, and Commercial Model D. We pass the same reference image to each system and obtain the corresponding assets. We use a target polygon count of 23K.

9.1 AssetBench: General Object Generation

To assess the quality of generated assets across diverse categories, we introduce AssetBench, a benchmark of 101 high-quality 3D assets manually curated and reviewed by technical artists. The dataset spans diverse

Table 8 Ablation study of latency improvements evaluated on a representative test asset. Each row reports the latency after cumulatively applying the corresponding optimization.

MeshGen + Geometry		TextureGen	
Stage	Lat. (s)	Stage	Lat. (s)
Baseline	103.15	Baseline	117.68
+ CuMesh	78.15	+ Prog. Distillation	41.42
+ Prog. Distillation	53.10	+ FA3 + compile	31.21
+ FA3 + compile	32.79	+ Precompute backproject data	27.11
+ I/O optimization	27.97	+ Rendering optimization	23.23
+ Parallel UV unwrap	21.09	+ Dual-GPU CFG branch split	17.85
+ DRTK normal baking	12.25		

categories including vehicles, daily-use objects, animals, and some characters. For each sample, we render an isometric/frontal reference view of the ground-truth 3D asset, which serves as the image prompt for all evaluated methods.

We evaluate image-to-3D generation along two axes. Shape quality is measured using *Chamfer Distance (CD)*, the symmetric Chamfer Distance between uniformly sampled surface points after unit-cube normalization and ICP alignment over 24 canonical orientations with gradient-based refinement, and *Volumetric IoU*, the occupancy IoU estimated from 10^5 uniformly sampled points in $[-0.5, 0.5]^3$ after the same ICP alignment. Faithfulness to the image prompt is measured using *VLM-as-a-Judge*, where a VLM extracts attribute-value pairs from the reference image, converts them into binary verification questions, and answers each question for 9 rendered views; we score *yes/partially/no* as 1/0.5/0 and average over questions and views (Duggal et al., 2025; Hu et al., 2023), and *CLIP Similarity*, the mean CLIP ViT-L/14 cosine similarity between generated and ground-truth renders from 9 uniformly spaced rendered views of the generated mesh.

Table 9 Quantitative results on AssetBench. The best values are highlighted in **bold** and the second-best are underlined. Arrows indicate whether higher (\uparrow) or lower (\downarrow) values are optimal.

Method	Shape Quality		Fidelity	
	IoU \uparrow	CD \downarrow	VLM \uparrow	CLIP \uparrow
AssetGen	0.4985	<u>0.0098</u>	0.7048	0.8993
AssetGen Flash	<u>0.4997</u>	<u>0.0098</u>	<u>0.6977</u>	<u>0.8978</u>
Commercial Model A	0.4993	0.0102	0.6921	0.8826
Commercial Model B	0.5298	0.0087	0.6500	0.8610
Commercial Model C	0.4522	0.0103	0.6482	0.8528
Commercial Model D	0.4849	0.0119	0.6905	0.8869

Results. Table 9 shows a clear split between geometry and appearance/reference fidelity. Commercial Model B leads the volumetric geometry metrics, with the best IoU and Chamfer Distance, indicating the strongest geometric reconstruction among the evaluated baselines. AssetGen is close on geometry while leading the reference-fidelity metrics, achieving the highest VLM verification score and GT-CLIP similarity. This suggests that AssetGen’s main advantage is not a uniformly stronger geometry prior, but a stronger end-to-end asset pipeline for preserving reference appearance and producing textured assets at much lower latency.

9.2 CharacterBench: Character Generation

CharacterBench is a benchmark of 100 character reference images designed to evaluate image-to-3D generation for characters. Unlike AssetBench, no ground-truth meshes are provided. Instead, the evaluation focuses on perceptual quality dimensions uniquely challenging for character generation—facial likeness, anatomical hand correctness, and full-body fidelity to the reference—using specialized VLM-based and CLIP-based protocols.

Metrics. We evaluate along four character-specific axes. First, we assess the quality of the generated face. We first select a VLM-verified camera distance that keeps the full face visible, then evaluate frontal and profile

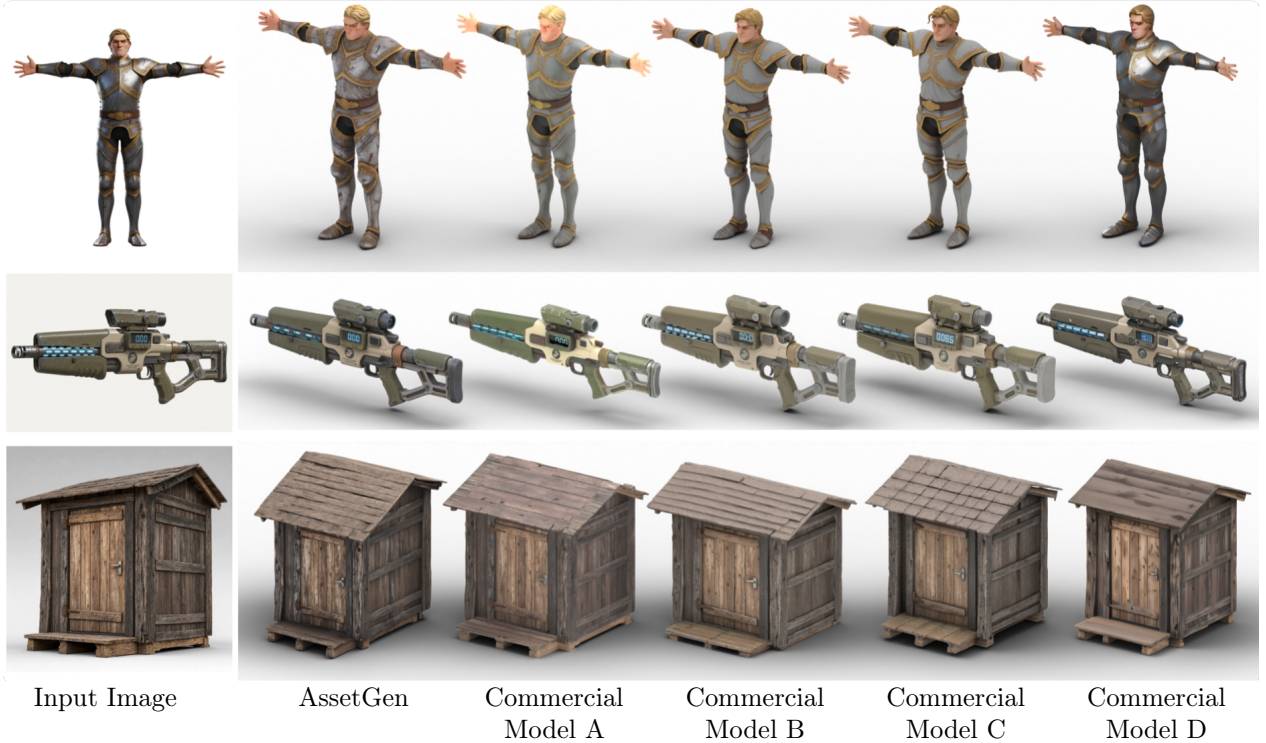


Figure 6 Qualitative comparison against commercial baselines. From left to right: the input image, AssetGen, Commercial Model A, Commercial Model B, Commercial Model C, and Commercial Model D.

Table 10 Quantitative results for character generation on CharacterBench. The best value in each column is highlighted in **bold** and the second-best are underlined. All metrics favor higher values (\uparrow).

Method	Face Quality		Face Fidelity		Hand	Overall Fidelity	
	Frontal	Profile	Face CLIP	Face Ref	Finger	Ref Fid	CLIP
AssetGen	0.748	0.196	0.838	0.893	0.784	0.903	<u>0.777</u>
AssetGen Flash	0.554	0.191	0.822	0.888	0.773	<u>0.901</u>	0.780
Commercial Model A	0.558	0.219	0.812	0.882	0.732	0.895	0.772
Commercial Model B	<u>0.695</u>	0.230	<u>0.832</u>	<u>0.890</u>	0.948	<u>0.901</u>	0.767
Commercial Model C	0.590	0.230	0.814	0.879	<u>0.928</u>	0.891	0.761

renders of the face. *Frontal Face Score* uses a VLM to check frontal renders for symmetry, natural expression, correct eye count and placement, mouth-nose alignment, and absence of blurred facial regions. A separate eye-quality rubric evaluates each eye for asymmetry and blur. The final score averages the normalized QA score and the eye score. *Profile Face Score* evaluates left and right profile renders for texture artifacts, ear visibility, and clean face/non-face boundaries. Scores are averaged across both profiles, and eye evaluation is omitted because profile occlusion makes it unreliable.

Next, we evaluate face fidelity relative to the reference identity. *Face CLIP Similarity* segments the reference face with SAM3 (Carion et al., 2025), crops rendered frontal faces from three views using per-pixel face-index maps, and averages CLIP ViT-L/14 cosine similarity between the reference crop and rendered crops. *Face Reference Fidelity* uses VLM-generated verification questions to assess facial attributes such as features, colors, proportions, and markings. The VLM verifies these questions on rendered views.

We also evaluate the quality of the generated *hands*. *Finger Score* renders each hand from multiple views, segments candidate regions, and uses a VLM to classify each region as finger or non-finger. View counts are aggregated by majority vote when the palm faces the camera, and by maximum count otherwise to account for occlusion. The score penalizes missing and hallucinated fingers symmetrically.



Figure 7 Qualitative comparison between AssetGen and Trellis 2. AssetGen preserves fine details more faithfully, as shown by the legible texts on the gas pump (“GAS” “DANGE”) and intricate details of the character’s body and facial components.



Figure 8 AssetGen qualitative gallery featuring sand-themed assets. This default configuration utilizes the two-stage MeshGen pipeline and high-fidelity TextureGen to prioritize visual quality, delivering production-ready assets in approximately 30 seconds end-to-end.

Finally, we evaluate full-body correspondence to the input reference. *Reference Fidelity* applies the same verification-question protocol to clothing, proportions, accessories, materials, and markings, reporting the fraction of correctly answered questions. Questions are generated by a VLM. *CLIP Image Similarity* computes the mean CLIP ViT-L/14 cosine similarity between the input reference image and 24 rendered views, excluding top and bottom views.

Results. Table 10 reports character-specific metrics on CharacterBench. AssetGen achieves the best frontal face quality (0.748) and leads both face-fidelity metrics, Face CLIP (0.838) and Face Ref (0.893), indicating strong preservation of the reference identity. AssetGen also obtains the highest overall reference-fidelity score (0.903), reflecting better consistency in clothing, accessories, proportions, and markings. The clearest remaining gap is hand structure: Commercial Model B achieves the highest finger score, showing a stronger hand-geometry prior. AssetGen (Flash) remains close to the default configuration on reference-fidelity metrics and slightly improves full-body CLIP similarity, consistent with its role as a faster configuration that preserves usable visual quality.

9.3 Human Evaluation

We further conduct a blind human evaluation on 195 image-conditioned assets spanning general objects, characters, buildings, and other common asset categories. To reduce bias from benchmark construction, the input images were collected by artists, who were asked to provide diverse concept images they considered useful for 3D asset creation. We did not select or inspect these images during benchmark construction. Evaluators inspect each generated result in an interactive 3D viewer with access to the final mesh, texture, UV layout,



Figure 9 AssetGen qualitative gallery featuring ice-themed assets.



Figure 10 AssetGen (Flash) qualitative gallery featuring magic forest assets.

and wireframe. We do not use turntable videos or fixed rendered views for this study; the goal is to evaluate the asset itself under direct inspection. Method identity is hidden from annotators.

Each asset is scored on an absolute 1–5 scale, where 1 indicates a severe failure and 5 indicates an excellent result. We group the rubric into three categories. *General quality* averages prompt adherence, style adherence, usability, and aesthetic quality. *Geometry quality* averages distortion, proportion, contiguity, accuracy, scale, alignment, topology, and UV layout. Geometry is evaluated on the final simplified mesh for all methods, matching the representation that would be used downstream. *Texture quality* averages consistency, accuracy of materials and shapes, clarity of details and patterns, and visible artifacts. Category scores are computed as the mean over their respective sub-criteria.

Table 11 shows that AssetGen receives the highest average score in all three categories. The margins are modest rather than overwhelming, which is the right interpretation for a strong commercial baseline: the main result is that the default AssetGen path reaches comparable-to-better inspected asset quality while operating at much lower end-to-end latency. Flash remains close to Commercial Model A on general and geometry quality while trailing the full AssetGen model, reflecting the intended quality-responsiveness trade-off.

Table 11 Blind human evaluation across 195 assets. All scores are reported on an absolute 1–5 scale (↑ higher is better). The general, geometry, and texture ratings represent averages over the specific subcriteria defined in [section 9.3](#). Note that geometry quality is evaluated directly on each method’s final simplified mesh.

Method	General ↑	Geometry ↑	Texture ↑
AssetGen	2.80	2.96	2.68
AssetGen Flash	2.63	2.88	2.55
Commercial Model A	2.61	2.86	2.58

10 Qualitative Results

In this section, we present qualitative results that complement the quantitative evaluation. We include matched comparisons with commercial systems, a comparison with Trellis 2 (Xiang et al., 2025a), galleries from the default AssetGen configuration and the faster AssetGen (Flash) configuration, and examples on real-world images.

Qualitative comparison. [figure 6](#) compares AssetGen against Commercial Model A, Commercial Model B, Commercial Model C, and Commercial Model D under matched input and rendering conditions. All methods are evaluated without PBR materials. Overall, the commercial baselines are strong and produce compelling assets. Commercial Model B often produces the strongest geometry, consistent with our quantitative results. AssetGen produces competitive geometry while generally showing cleaner and richer textures, and stronger reference-image fidelity.

Comparison with Trellis 2. [figure 7](#) compares AssetGen with Trellis 2, a strong open-source image-to-3D baseline. We use the Trellis 2 output as recommended and keep its final mesh at one million polygons. This is a much denser representation than AssetGen, whose outputs are simplified to about 23K. At the Trellis 2 scale, UV unwrapping alone can take close to a minute. Qualitatively, Trellis 2 is less robust than AssetGen and the commercial baselines on complex inputs. For example, in the second example, Trellis 2 fails to recover the letters cleanly; and in the third example, the fingers are distorted despite the high polygon count.

AssetGen gallery. [figure 8](#) and [figure 9](#) show generations from the default AssetGen configuration. Both the input images and the 3D meshes are single-shot generations without cherry picking.

AssetGen (Flash) gallery. [figure 10](#) shows results from AssetGen (Flash). Both the input images and the 3D meshes are single-shot generations without cherry picking.

Real-World Inputs [figure 11](#) shows qualitative examples on real-world photographs. These examples suggest that the same image-to-asset pipeline can also produce plausible textured meshes from real-world inputs, even though the model is trained primarily on synthetic 3D data. For example, in the second column, AssetGen recovers a complete bucket shape despite partial occlusion, illustrating how its learned shape prior can plausibly complete unseen regions.

11 Conclusion and Limitations

AssetGen provides a practical path from a single reference image to an explicit textured 3D asset. The default AssetGen configuration produces a simplified, UV-unwrapped, normal-baked textured mesh in approximately 30 seconds on H100 GPUs. AssetGen (Flash) runs in approximately 14 seconds in our measured deployment, providing a faster operating point for rapid exploration, preview, and agentic workflows. Through extensive quantitative evaluation, qualitative comparison, and blind human inspection, we show that AssetGen is competitive in asset quality with leading commercial image-to-3D systems while substantially reducing user-facing generation time.

While our results demonstrate a fast and deployable asset generation pipeline, several limitations remain:

Single-image ambiguity. Single-image 3D generation is inherently underconstrained. The model must infer



Figure 11 Asset generation from real-world images. Each column displays an in-the-wild input photograph alongside two rendered views of the resulting AssetGen mesh. These examples demonstrate the pipeline’s robustness to natural lighting, background clutter, and partial occlusion.

occluded surfaces, which can fail for rare categories, unusual viewpoints, asymmetric objects, or complex back-side structure. Symmetric objects are generally more reliable; irregular chairs, sculptures, and objects with hidden mechanical parts remain more challenging.

Topology constraints. Marching-cubes extraction produces arbitrary triangle meshes. The simplification pipeline preserves surface fidelity and keeps assets lightweight, but it does not enforce clean topology, artist-friendly edge flow, skeletal rigging constraints, or animation-ready deformation behavior. Assets intended for rigged characters may still require retopology.

Rigging and animation. Static textured meshes are only one step toward interactive characters. Integrating auto-rigging, skin-weight prediction, blend-shape generation, and motion synthesis would close the gap between generated assets and animated avatars, but these tasks require topology-aware reasoning and scarce rigged training data.

References

- Jason Ansel, Edward Yang, Horace He, Natalia Gimelshein, Animesh Jain, Michael Voznesensky, Bin Bao, Peter Bell, David Berard, Evgeni Burovski, et al. Pytorch 2: Faster machine learning through dynamic python bytecode transformation and graph compilation. In *Proceedings of the 29th ACM international conference on architectural support for programming languages and operating systems, volume 2*, pages 929–947, 2024.
- Fan Bao, Shen Nie, Kaiwen Xue, Yue Cao, Chongxuan Li, Hang Su, and Jun Zhu. All are worth words: A vit backbone for diffusion models. In *Proc. CVPR*, pages 22669–22679, 2023.
- Gavin Barill, Neil G Dickson, Ryan Schmidt, David IW Levin, and Alec Jacobson. Fast winding numbers for soups and clouds. *ACM Trans. on Graphics (TOG)*, 37(4):1–12, 2018.
- Raphael Bensadoun, Yanir Kleiman, Idan Azuri, Omri Harosh, Andrea Vedaldi, Natalia Neverova, and Oran Gafni. Meta 3d texturegen: Fast and consistent texture generation for 3d objects. *arXiv preprint arXiv:2407.02430*, 2024.
- Mark Boss, Zixuan Huang, Aaryaman Vasishtha, and Varun Jampani. Sf3d: Stable fast 3d mesh reconstruction with uv-unwrapping and illumination disentanglement. In *Proc. CVPR*, pages 16240–16250, 2025.
- ByteDance Seed3D Team. Seed3d 2.0: Advancing high-fidelity simulation-ready 3D content generation. 2026.
- Nicolas Carion, Laura Gustafson, Yuan-Ting Hu, Shoubhik Debnath, Ronghang Hu, Didac Suris, Chaitanya Ryali, Kalyan Vasudev Alwala, Haitham Khedr, Andrew Huang, et al. Sam 3: Segment anything with concepts. *arXiv preprint arXiv:2511.16719*, 2025.
- Eric R Chan, Connor Z Lin, Matthew A Chan, Koki Nagano, Boxiao Pan, Shalini De Mello, Orazio Gallo, Leonidas J Guibas, Jonathan Tremblay, Sameh Khamis, et al. Efficient geometry-aware 3d generative adversarial networks. In *Proc. CVPR*, pages 16123–16133, 2022.
- Dave Zhenyu Chen, Yawar Siddiqui, Hsin-Ying Lee, Sergey Tulyakov, and Matthias Nießner. Text2tex: Text-driven texture synthesis via diffusion models. In *Proc. ICCV*, pages 18558–18568, 2023.
- Lei Chen, Yuan Meng, Chen Tang, Xinzhu Ma, Jingyan Jiang, Xin Wang, Zhi Wang, and Wenwu Zhu. Q-dit: Accurate post-training quantization for diffusion transformers. In *Proc. CVPR*, pages 28306–28315, 2025a.
- Zhaoxi Chen, Jiayang Tang, Yuhao Dong, Ziang Cao, Fangzhou Hong, Yushi Lan, Tengfei Wang, Haozhe Xie, Tong Wu, Shunsuke Saito, et al. 3dtopia-xl: Scaling high-quality 3d asset generation via primitive diffusion. In *Proc. CVPR*, pages 26576–26586, 2025b.
- Wei Cheng, Juncheng Mu, Xianfang Zeng, Xin Chen, Anqi Pang, Chi Zhang, Zhibin Wang, Bin Fu, Gang Yu, Ziwei Liu, et al. Mvpaint: Synchronized multi-view diffusion for painting anything 3d. In *Proc. CVPR*, pages 585–594, 2025.
- Jonathan Cohen, Marc Olano, and Dinesh Manocha. Appearance-preserving simplification. In *Proceedings of the 25th annual conference on Computer graphics and interactive techniques*, pages 115–122, 1998.
- Tri Dao. Flashattention-2: Faster attention with better parallelism and work partitioning. In *Proc. ICLR*, 2024.
- Tri Dao, Dan Fu, Stefano Ermon, Atri Rudra, and Christopher Ré. Flashattention: Fast and memory-efficient exact attention with io-awareness. In *Proc. NeurIPS*, 2022.
- Timothée Darcet, Maxime Oquab, Julien Mairal, and Piotr Bojanowski. Vision transformers need registers. In *Proc. ICLR*, 2024.
- Christopher DeCoro and Natalya Tatarchuk. Real-time mesh simplification using the gpu. In *Proceedings of the 2007 symposium on Interactive 3D graphics and games*, pages 161–166, 2007.
- Shivam Duggal, Yushi Hu, Oscar Michel, Aniruddha Kembhavi, William T Freeman, Noah A Smith, Ranjay Krishna, Antonio Torralba, Ali Farhadi, and Wei-Chiu Ma. Eval3d: Interpretable and fine-grained evaluation for 3d generation. In *Proc. CVPR*, pages 13326–13336, 2025.
- Patrick Esser, Sumith Kulal, Andreas Blattmann, Rahim Entezari, Jonas Müller, Harry Saini, Yam Levi, Dominik Lorenz, Axel Sauer, Frederic Boesel, et al. Scaling rectified flow transformers for high-resolution image synthesis. In *Proc. ICML*, 2024.
- Weichen Fan, Amber Yijia Zheng, Raymond A. Yeh, and Ziwei Liu. CFG-Zero*: Improved classifier-free guidance for flow matching models. *arXiv preprint arXiv:2503.18886*, 2025.

- Xuhui Fan, Hongyu Wu, Longbing Cao, et al. Scot: Unifying consistency models and rectified flows via straight-consistent trajectories. *Proc. NeurIPS*, 38:141438–141465, 2026.
- Michael Garland and Paul S. Heckbert. Surface simplification using quadric error metrics. In *Proceedings of the 24th Annual Conference on Computer Graphics and Interactive Techniques*, pages 209–216, 1997.
- Zekun Hao, David W. Romero, Tsung-Yi Lin, and Ming-Yu Liu. Meshtron: High-fidelity, artist-like 3D mesh generation at scale. *arXiv preprint arXiv:2412.09548*, 2024.
- Jon Hasselgren, Zheng Zeng, Milos Hasan, and Jacob Munkberg. VideoMatGen: PBR materials through joint generative modeling. *arXiv preprint arXiv:2603.16566*, 2026.
- Xianglong He, Zi-Xin Zou, Chia-Hao Chen, Yuan-Chen Guo, Ding Liang, Chun Yuan, Wanli Ouyang, Yan-Pei Cao, and Yangguang Li. Sparseflex: High-resolution and arbitrary-topology 3d shape modeling. In *Proc. ICCV*, pages 14822–14833, 2025.
- Yihui He, Rui Yan, Katerina Fragkiadaki, and Shoou-I Yu. Epipolar transformers. In *Proc. CVPR*, pages 7779–7788, 2020.
- Jonathan Ho and Tim Salimans. Classifier-free diffusion guidance. *arXiv preprint arXiv:2207.12598*, 2022.
- Hugues Hoppe. Progressive meshes. In *Seminal Graphics Papers: Pushing the Boundaries, Volume 2*, pages 111–120, 2023.
- Yushi Hu, Benlin Liu, Jungo Kasai, Yizhong Wang, Mari Ostendorf, Ranjay Krishna, and Noah A Smith. Tifa: Accurate and interpretable text-to-image faithfulness evaluation with question answering. In *Proc. ICCV*, pages 20406–20417, 2023.
- Jingwei Huang, Yichao Zhou, and Leonidas Guibas. Manifoldplus: A robust and scalable watertight manifold surface generation method for triangle soups. *arXiv preprint arXiv:2005.11621*, 2020.
- Xin Huang, Tengfei Wang, Ziwei Liu, and Qing Wang. Material anything: Generating materials for any 3d object via diffusion. In *Proc. CVPR*, pages 26556–26565, 2025a.
- Zixuan Huang, Mark Boss, Aaryaman Vasishta, James M Rehg, and Varun Jampani. Spar3d: Stable point-aware reconstruction of 3d objects from single images. In *Proc. CVPR*, 2025b.
- Team Hunyuan3D, Shuhui Yang, Mingxin Yang, Yifei Feng, Xin Huang, Sheng Zhang, Zebin He, Di Luo, Haolin Liu, Yunfei Zhao, et al. Hunyuan3d 2.1: From images to high-fidelity 3d assets with production-ready pbr material. *arXiv preprint arXiv:2506.15442*, 2025.
- Bernhard Kerbl, Georgios Kopanas, Thomas Leimkühler, and George Drettakis. 3D gaussian splatting for real-time radiance field rendering. *ACM Trans. on Graphics (TOG)*, 42(4), 2023.
- Nikita Kornilov, Petr Mokrov, Alexander Gasnikov, and Alexander Korotin. Optimal flow matching: Learning straight trajectories in just one step. *Proc. NeurIPS*, 37:104180–104204, 2024.
- Zeqiang Lai, Yunfei Zhao, Zibo Zhao, Haolin Liu, Qingxiang Lin, Jingwei Huang, Chunchao Guo, and Xiangyu Yue. Lattice: Democratize high-fidelity 3d generation at scale. *arXiv preprint arXiv:2512.03052*, 2025a.
- Zeqiang Lai, Yunfei Zhao, Zibo Zhao, Haolin Liu, Fuyun Wang, Huiwen Shi, Xianghui Yang, Qingxiang Lin, Jingwei Huang, Yuhong Liu, et al. Unleashing vecset diffusion model for fast shape generation. In *Proc. ICCV*, pages 2523–2533, 2025b.
- Samuli Laine, Janne Hellsten, Tero Karras, Yeongho Seol, Jaakko Lehtinen, and Timo Aila. Modular primitives for high-performance differentiable rendering. *ACM Trans. on Graphics (TOG)*, 39(6), 2020.
- Biwen Lei, Yang Li, Xinhai Liu, Shuhui Yang, Lixin Xu, Jingwei Huang, Ruining Tang, Haohan Weng, Jian Liu, Jing Xu, et al. Hunyuan3d studio: End-to-end ai pipeline for game-ready 3d asset generation. *arXiv preprint arXiv:2509.12815*, 2025.
- Jiabao Lei, Kewei Shi, Zhihao Liang, and Kui Jia. Armesh: Autoregressive mesh generation via next-level-of-detail prediction. *Proc. NeurIPS*, 38:161613–161633, 2026.
- Bruno Lévy, Sylvain Petitjean, Nicolas Ray, and Jérôme Maillot. Least squares conformal maps for automatic texture atlas generation. In *Seminal Graphics Papers: Pushing the Boundaries, Volume 2*, pages 193–202, 2023.

- Peng Li, Yuan Liu, Xiaoxiao Long, Feihu Zhang, Cheng Lin, Mengfei Li, Xingqun Qi, Shanghang Zhang, Wenhan Luo, Ping Tan, et al. Era3d: High-resolution multiview diffusion using efficient row-wise attention. In *Proc. NeurIPS*, 2024.
- Yanfeng Li, Tao Tan, Qinquan Gao, Zhiwen Cao, Xiaohong Liu, and Yue Sun. Hifi-mesh: High-fidelity efficient 3d mesh generation via compact autoregressive dependence. In *Proc. AAAI*, volume 40, pages 6566–6574, 2026.
- Yangguang Li, Zi-Xin Zou, Zexiang Liu, Dehu Wang, Yuan Liang, Zhipeng Yu, Xingchao Liu, Yuan-Chen Guo, Ding Liang, Wanli Ouyang, et al. Triposg: High-fidelity 3d shape synthesis using large-scale rectified flow models. *IEEE Transactions on Pattern Analysis and Machine Intelligence*, 2025.
- Shanchuan Lin, Bingchen Liu, Jiashi Li, and Xiao Yang. Common diffusion noise schedules and sample steps are flawed. In *Proc. WACV*, pages 5404–5411, 2024.
- Peter Lindstrom and Greg Turk. Fast and memory efficient polygonal simplification. In *Proceedings Visualization'98 (Cat. No. 98CB36276)*, pages 279–286. IEEE, 1998.
- Stefan Lionar, Jiabin Liang, and Gim Hee Lee. Treemeshgpt: Artistic mesh generation with autoregressive tree sequencing. In *Proc. CVPR*, pages 26608–26617, 2025.
- Ruoshi Liu, Rundi Wu, Basile Van Hoorick, Pavel Tokmakov, Sergey Zakharov, and Carl Vondrick. Zero-1-to-3: Zero-shot one image to 3d object. In *Proc. ICCV*, pages 9298–9309, 2023a.
- Xingchao Liu, Chengyue Gong, and Qiang Liu. Flow straight and fast: Learning to generate and transfer data with rectified flow. *arXiv preprint arXiv:2209.03003*, 2022.
- Xingchao Liu, Xiwen Zhang, Jianzhu Ma, Jian Peng, et al. InstafLOW: One step is enough for high-quality diffusion-based text-to-image generation. In *Proc. ICLR*, 2023b.
- Yuan Liu, Cheng Lin, Zijiao Zeng, Xiaoxiao Long, Lingjie Liu, Taku Komura, and Wenping Wang. Syncdreamer: Generating multiview-consistent images from a single-view image. In *Proc. ICLR*, 2024.
- Xiaoxiao Long, Yuan-Chen Guo, Cheng Lin, Yuan Liu, Zhiyang Dou, Lingjie Liu, Yuexin Ma, Song-Hai Zhang, Marc Habermann, Christian Theobalt, et al. Wonder3d: Single image to 3d using cross-domain diffusion. In *Proc. CVPR*, 2024.
- Ilya Loshchilov and Frank Hutter. Decoupled weight decay regularization. *arXiv preprint arXiv:1711.05101*, 2017.
- Guan Luo, Xiu Li, Rui Chen, Xuanyu Yi, Jing Lin, Chia-Hao Chen, Jiahang Liu, Song-Hai Zhang, and Jianfeng Zhang. Topomesh: High-fidelity mesh autoencoding via topological unification. *arXiv preprint arXiv:2603.24278*, 2026.
- Chenlin Meng, Robin Rombach, Ruiqi Gao, Diederik Kingma, Stefano Ermon, Jonathan Ho, and Tim Salimans. On distillation of guided diffusion models. In *Proc. CVPR*, pages 14297–14306, 2023.
- Lars Mescheder, Michael Oechsle, Michael Niemeyer, Sebastian Nowozin, and Andreas Geiger. Occupancy networks: Learning 3d reconstruction in function space. In *Proc. CVPR*, pages 4460–4470, 2019.
- Ben Mildenhall, Pratul P Srinivasan, Matthew Tancik, Jonathan T Barron, Ravi Ramamoorthi, and Ren Ng. Nerf: Representing scenes as neural radiance fields for view synthesis. *Commun. ACM*, 65(1):99–106, 2021.
- Thomas Müller, Alex Evans, Christoph Schied, and Alexander Keller. Instant neural graphics primitives with a multiresolution hash encoding. *ACM Trans. on Graphics (TOG)*, 41(4):1–15, 2022.
- Richard A Newcombe, Shahram Izadi, Otmar Hilliges, David Molyneaux, David Kim, Andrew J Davison, Pushmeet Kohi, Jamie Shotton, Steve Hodges, and Andrew Fitzgibbon. Kinectfusion: Real-time dense surface mapping and tracking. In *2011 10th IEEE international symposium on mixed and augmented reality*, pages 127–136. Ieee, 2011.
- Seonghun Oh, Xiaodi Yuan, Xinyue Wei, Ruoxi Shi, Fanbo Xiang, Minghua Liu, and Hao Su. Pamo: Parallel mesh optimization for intersection-free low-poly modeling on the gpu. In *Computer Graphics Forum*, volume 44, page e70267. Wiley Online Library, 2025.
- Maxime Oquab, Timothée Darcet, Théo Moutakanni, Huy Vo, Marc Szafraniec, Vasil Khalidov, Pierre Fernandez, Daniel Haziza, Francisco Massa, Alaaeldin El-Nouby, et al. Dinov2: Learning robust visual features without supervision. *arXiv preprint arXiv:2304.07193*, 2023.
- Jeong Joon Park, Peter Florence, Julian Straub, Richard Newcombe, and Steven Lovegrove. DeepSDF: Learning continuous signed distance functions for shape representation. In *Proc. CVPR*, pages 165–174, 2019.

- Steven G. Parker, James Bigler, Andreas Dietrich, Heiko Friedrich, Jared Hoberock, David Luebke, David McAllister, Morgan McGuire, Keith Morley, Austin Robison, and Martin Stich. OptiX: A general purpose ray tracing engine. *ACM Trans. on Graphics (TOG)*, 29(4), 2010.
- William Peebles and Saining Xie. Scalable diffusion models with transformers. In *Proc. ICCV*, pages 4195–4205, 2023.
- Stanislav Pidhorskyi, Tomas Simon, Gabriel Schwartz, He Wen, Yaser Sheikh, and Jason Saragih. Rasterized edge gradients: Handling discontinuities differentiably. In *Proc. ECCV*, pages 335–352. Springer, 2024.
- Ben Poole, Ajay Jain, Jonathan T Barron, and Ben Mildenhall. Dreamfusion: Text-to-3d using 2d diffusion. *arXiv*, 2022.
- Nikhila Ravi, Jeremy Reizenstein, David Novotny, Taylor Gordon, Wan-Yen Lo, Justin Johnson, and Georgia Gkioxari. Accelerating 3d deep learning with pytorch3d. *arXiv*, 2020.
- Elad Richardson, Gal Metzger, Yuval Alaluf, Raja Giryes, and Daniel Cohen-Or. Texture: Text-guided texturing of 3d shapes. In *ACM SIGGRAPH 2023 conference proceedings*, pages 1–11, 2023.
- Tim Salimans and Jonathan Ho. Progressive distillation for fast sampling of diffusion models. In *Proc. ICLR*, 2022.
- Aditya Sanghi, Aliasghar Khani, Pradyumna Reddy, Arianna Rampini, Derek Cheung, Kamal Rahimi Malekshan, Kanika Madan, and Hooman Shayani. Wavelet latent diffusion (wala): Billion-parameter 3d generative model with compact wavelet encodings. *arXiv preprint arXiv:2411.08017*, 2024.
- Nikolaos Sarafianos, Tuur Stuyck, Xiaoyu Xiang, Yilei Li, Jovan Popovic, and Rakesh Ranjan. Garment3dgen: 3d garment stylization and texture generation. In *2025 International Conference on 3D Vision (3DV)*, pages 1382–1393. IEEE, 2025.
- Axel Sauer, Dominik Lorenz, Andreas Blattmann, and Robin Rombach. Adversarial diffusion distillation. In *Proc. ECCV*, pages 87–103. Springer, 2024.
- Jay Shah, Ganesh Bikshandi, Ying Zhang, Vijay Thakkar, Pradeep Ramani, and Tri Dao. Flashattention-3: Fast and accurate attention with asynchrony and low-precision. *Proc. NeurIPS*, 37:68658–68685, 2024.
- Mingqi Shao, Feng Xiong, Zhaoxu Sun, and Mu Xu. Mvpainter: Accurate and detailed 3d texture generation via multi-view diffusion with geometric control. *arXiv preprint arXiv:2505.12635*, 2025.
- Noam Shazeer. Glu variants improve transformer. *arXiv preprint arXiv:2002.05202*, 2020.
- Alla Sheffer, Bruno Lévy, Maxim Mogilnitsky, and Alexander Bogomyakov. ABF++: Fast and robust angle based flattening. *ACM Trans. on Graphics (TOG)*, 24(2):311–330, 2005.
- Yichun Shi, Peng Wang, Jianglong Ye, Long Mai, Kejie Li, and Xiao Yang. Mvdream: Multi-view diffusion for 3d generation. In *Proc. ICLR*, 2024.
- Yawar Siddiqui, Antonio Alliegro, Alexey Artemov, Tatiana Tommasi, Daniele Sirigatti, Vladislav Rosov, Angela Dai, and Matthias Nießner. Meshgpt: Generating triangle meshes with decoder-only transformers. In *Proc. CVPR*, pages 19615–19625, 2024.
- Alvy Ray Smith. Tint Fill. In *Proc. SIGGRAPH*, 1979.
- Yang Song, Prafulla Dhariwal, Mark Chen, and Ilya Sutskever. Consistency models. In *Proc. ICML*, pages 32211–32252, 2023.
- Shitao Tang, Fuyang Zhang, Jiacheng Chen, Peng Wang, and Yasutaka Furukawa. Mvdiffusion: Enabling holistic multi-view image generation with correspondence-aware diffusion. *Proc. NeurIPS*, 2023.
- Shitao Tang, Jiacheng Chen, Dilin Wang, Chengzhou Tang, Fuyang Zhang, Yuchen Fan, Vikas Chandra, Yasutaka Furukawa, and Rakesh Ranjan. Mvdiffusion++: A dense high-resolution multi-view diffusion model for single or sparse-view 3d object reconstruction. In *Proc. ECCV*, pages 175–191. Springer, 2024.
- Dmitry Tochilkin, David Pankratz, Zexiang Liu, Zixuan Huang, Adam Letts, Yanguang Li, Ding Liang, Christian Laforte, Varun Jampani, and Yan-Pei Cao. Triposr: Fast 3d object reconstruction from a single image. *arXiv preprint arXiv:2403.02151*, 2024.
- Alexander Tong, Kilian Fatras, Nikolay Malkin, Guillaume Hugué, Yanlei Zhang, Jarrid Rector-Brooks, Guy Wolf, and Yoshua Bengio. Improving and generalizing flow-based generative models with minibatch optimal transport. *arXiv preprint arXiv:2302.00482*, 2023.

- Vikram Voleti, Chun-Han Yao, Mark Boss, Adam Letts, David Pankratz, Dmitry Tochilkin, Christian Laforte, Robin Rombach, and Varun Jampani. Sv3d: Novel multi-view synthesis and 3d generation from a single image using latent video diffusion. In *Proc. ECCV*, pages 439–457. Springer, 2024.
- Hanxiao Wang, Yuan-Chen Guo, Ying-Tian Liu, Zi-Xin Zou, Biao Zhang, Weize Quan, Ding Liang, Yan-Pei Cao, and Dong-Ming Yan. Face: A face-based autoregressive representation for high-fidelity and efficient mesh generation. *arXiv preprint arXiv:2603.01515*, 2026.
- Zhengyi Wang, Cheng Lu, Yikai Wang, Fan Bao, Chongxuan Li, Hang Su, and Jun Zhu. Prolificdreamer: High-fidelity and diverse text-to-3d generation with variational score distillation. In *Proc. NeurIPS*, 2023.
- Zhengyi Wang, Yikai Wang, Yifei Chen, Chendong Xiang, Shuo Chen, Dajiang Yu, Chongxuan Li, Hang Su, and Jun Zhu. Crm: Single image to 3d textured mesh with convolutional reconstruction model. In *Proc. ECCV*, pages 57–74. Springer, 2024.
- Shuang Wu, Youtian Lin, Feihu Zhang, Yifei Zeng, Jingxi Xu, Philip Torr, Xun Cao, and Yao Yao. Direct3d: Scalable image-to-3d generation via 3d latent diffusion transformer. In *Proc. NeurIPS*, 2024.
- Jianfeng Xiang, Xiaoxue Chen, Sicheng Xu, Ruicheng Wang, Zelong Lv, Yu Deng, Hongyuan Zhu, Yue Dong, Hao Zhao, Nicholas Jing Yuan, and Jiaolong Yang. Native and compact structured latents for 3d generation. *arXiv preprint arXiv: 2512.14692*, 2025a.
- Jianfeng Xiang, Zelong Lv, Sicheng Xu, Yu Deng, Ruicheng Wang, Bowen Zhang, Dong Chen, Xin Tong, and Jiaolong Yang. Structured 3d latents for scalable and versatile 3d generation. In *Proc. CVPR*, pages 21469–21480, 2025b.
- Xiaoyu Xiang, Liat Sless Gorelik, Yuchen Fan, Omri Armstrong, Forrest Iandola, Yilei Li, Ita Lifshitz, and Rakesh Ranjan. Make-a-texture: Fast shape-aware texture generation in 3 seconds. In *Proc. WACV*, 2025c.
- Duoteng Xu, Yuguang Chen, Jing Li, Xinhai Liu, Xueqi Ma, Zhuo Chen, Dongyu Zhang, and Chunchao Guo. Seamcrafter: Enhancing mesh seam generation for artist uv unwrapping via reinforcement learning. *arXiv preprint arXiv:2509.20725*, 2025.
- Jiale Xu, Weihao Cheng, Yiming Gao, Xintao Wang, Shenghua Gao, and Ying Shan. Instantmesh: Efficient 3d mesh generation from a single image with sparse-view large reconstruction models. *arXiv preprint arXiv:2404.07191*, 2024.
- Rui Xu, Dafei Qin, Kaichun Qiao, Qiuji Dong, Huaijin Pi, Qixuan Zhang, Longwen Zhang, Lan Xu, Jingyi Yu, Wenping Wang, et al. Strips as tokens: Artist mesh generation with native uv segmentation. *arXiv preprint arXiv:2604.09132*, 2026.
- Mengyu Yang, Yanming Yang, Chenyi Xu, Chenxi Song, Yufan Zuo, Tong Zhao, Ruibo Li, and Chi Zhang. Fast3dcache: Training-free 3d geometry synthesis acceleration. *arXiv preprint arXiv:2511.22533*, 2025.
- Hu Ye, Jun Zhang, Sibio Liu, Xiao Han, and Wei Yang. Ip-adapter: Text compatible image prompt adapter for text-to-image diffusion models. *arXiv preprint arXiv:2308.06721*, 2023.
- Tianwei Yin, Michaël Gharbi, Taesung Park, Richard Zhang, Eli Shechtman, Fredo Durand, and William T Freeman. Improved distribution matching distillation for fast image synthesis. In *Proc. NeurIPS*, 2024a.
- Tianwei Yin, Michaël Gharbi, Richard Zhang, Eli Shechtman, Fredo Durand, William T Freeman, and Taesung Park. One-step diffusion with distribution matching distillation. In *Proc. CVPR*, pages 6613–6623, 2024b.
- Jonathan Young. xatlas: Mesh parameterization / uv unwrapping library. <https://github.com/jpcy/xatlas>, 2023.
- Xianfang Zeng, Xin Chen, Zhongqi Qi, Wen Liu, Zibo Zhao, Zhibin Wang, Bin Fu, Yong Liu, and Gang Yu. Paint3d: Paint anything 3d with lighting-less texture diffusion models. In *Proc. CVPR*, pages 4252–4262, 2024.
- Biao Zhang, Jiapeng Tang, Matthias Niessner, and Peter Wonka. 3dshape2vecset: A 3d shape representation for neural fields and generative diffusion models. *ACM Trans. on Graphics (TOG)*, 42(4):1–16, 2023.
- Longwen Zhang, Ziyu Wang, Qixuan Zhang, Qiwei Qiu, Anqi Pang, Haoran Jiang, Wei Yang, Lan Xu, and Jingyi Yu. CLAY: A controllable large-scale generative model for creating high-quality 3D assets. *ACM Trans. on Graphics (TOG)*, 43(4), 2024.
- Ruowen Zhao, Junliang Ye, Zhengyi Wang, Guangce Liu, Yiwen Chen, Yikai Wang, and Jun Zhu. Deepmesh: Auto-regressive artist-mesh creation with reinforcement learning. In *Proc. ICCV*, 2025a.
- Zibo Zhao, Wen Liu, Xin Chen, Xianfang Zeng, Rui Wang, Pei Cheng, Bin Fu, Tao Chen, Gang Yu, and Shenghua Gao. Michelangelo: Conditional 3d shape generation based on shape-image-text aligned latent representation. In *Proc. NeurIPS*, 2023.

Zibo Zhao, Zeqiang Lai, Qingxiang Lin, Yunfei Zhao, Haolin Liu, Shuhui Yang, Yifei Feng, Mingxin Yang, Sheng Zhang, Xianghui Yang, et al. Hunyuan3d 2.0: Scaling diffusion models for high resolution textured 3d assets generation. *arXiv preprint arXiv:2501.12202*, 2025b.

Zhenyu Zhou, Defang Chen, Can Wang, Chun Chen, and Siwei Lyu. Dice: Distilling classifier-free guidance into text embeddings. In *Proc. AAAI*, 2026.

Haowei Zhu, Ji Liu, Ziqiong Liu, Dong Li, Junhai Yong, Bin Wang, and Emad Barsoum. Diffsparse: Accelerating diffusion transformers with learned token sparsity. *arXiv preprint arXiv:2604.03674*, 2026.